Chapter 6
Seismic Fragility Assessment of an Industrial Plant Substructure and Metastructures for Vibration Mitigation

Oreste S. Bursi

Abstract The tremendous impact of natural hazards, such as earthquakes, tsunamis, flooding, etc., which triggered technological accidents, referred to as natural-technological (NaTech) events, was demonstrated by several recent events as: (i) the Tohoku earthquake and the following Fukushima disaster in 2011; (ii) the Italian earthquakes in 2012 and 2016 which resulted in €42bn between direct and indirect costs, with casualties, thousands of displaced families, and affected business interruption that faced financial problems due non-existent or inadequate insurance. In addition to structural integrity, fitness for service of special risk industrial plants requires an understanding of specific threats, e.g. unrealistic design assumptions, insufficient controls at the construction stage, unexpected/unintended vibrations due to moving loads, etc. Therefore, measures to ensure safe operations depend on hazards and their relationships to the overall condition of the industrial plant. In this context, it is necessary to implement and support the Seveso-III Directive 2012/18/EU which regulates the control of major accident hazards involving dangerous substances and to extend the life and to ensure fitness for service of current special risk plants. To tackle this challenge the research conducted by the author and his coworkers involves a computational framework for an efficient and accurate seismic state-dependent fragility analysis. It is based on a combination of data acquired from an extensive experimental shake table test campaign on a full-scale prototype industrial steel frame structure and the most recent surrogate-based uncertainty quantification (UQ) forward analysis advancements. Specifically, the framework is applied to a real-world application consisting of seismic shake table tests of a representative industrial multistorey frame structure equipped with complex process components, carried out at the EUCENTRE facility in Italy, within the European SPIF project: Seismic Performance of Multi-component Systems in Special Risk Industrial Facilities. The results of this experimental research campaign also aspire to improve the understanding

O. S. Bursi (✉)
Department of Civil, Environmental and Mechanical Engineering, University of Trento, Via Mesiano 77, 38123 Trento, Italy
e-mail: oreste.bursi@unitn.it

V. Cozzani and F. Paolacci (eds.), *Management Strategies and Resilience Against NaTech Events*, CISM International Centre for Mechanical Sciences 616,
https://doi.org/10.1007/978-3-031-84485-0_6

of these complex systems and to improve the knowledge on FE modelling techniques. One goal aims to reduce the huge computational burden and to assess, as well, state-dependent fragility curves. Also innovative metamaterial-based solutions for disaster reduction in special risk facilities are proposed. To achieve this scope, the research builds upon the most recent innovative scientific and technological concepts developed within the research field of locally resonant phononic metamaterials. In particular, the feasibility of such metamaterial-based isolation concepts and systems is demonstrated across different low-frequency ranges, e.g. seismic waves. These general developments have further advanced through novel isolation concepts which can achieve negative effective mass and stiffness moduli in structures and through nonlinear mechanisms such as bistability. In sum, this research intends to conceive metastructures capable of rendering industrial plant equipment fully or partially isolated from the effects of incident waves impinging from all directions.

6.1 Introduction

6.1.1 Background and Motivation

Focusing on the industry world, from the last decade of major earthquake disasters, a key realisation has been that non-structural components (NSCs) of industrial plant facilities have been a significant driver for overall physical damage and disruption to business. To this scope, the Applied Technology Council (ATC) under the National Institute of Standards and Technology (NIST) invested in a year-long study to collect and document the body of available knowledge related to the seismic performance of NSCs, summarized in Rossi et al. (2020). From these studies, it clearly emerges: (i) a large adoption of classical load-and-resistance factor design (LRFD) and code-compliant methods often dated and inadequate, as highlighted also in Eads et al. (2013); (ii) a gap in performing fully comprehensive testing campaigns and investigations on coupling effects between primary structures and NSCs; (iii) a need to improve and enforce code requirements along with the development of reliable NSCs seismic demands models. In particular, codes and regulations establish the minimum requirements for structures to resist the effects of earthquakes with defined probability levels (or return periods), providing a basic level of seismic risk reduction. The primary objective of codes and regulations on structures is to save lives, not the structures themselves. When properly implemented, codes have significantly reduced the loss of life in major seismic events in recent years. However, from the perspective of economic resilience, the enormous scale of associated financial losses requires a paradigm shift. Encouragingly, in recent times, earthquake building codes have been revised to implement elements of a performance-based earthquake engineering (PBEE) framework to address issues of damage limitation and reparability as well as life safety. In this respect, the PBEE PEER framework has gained momentum above all to perform seismic risk analyses, thanks to its inherent versatility. Its

strength, indeed, relies on simple yet effective implementation of the total probability theorem, which allows to decouple and then combine the output of probabilistic seismic hazard analysis (PSHA) with fragility, damage, and loss analysis. To this end, the aforementioned fragility analysis step offers the critical link between seismic hazard and structural modelling, since it estimates the conditional probability of exceeding or attaining a certain damage state (DS) given an intensity measure (IM) of earthquake motion. In this regard, a growing number of studies, the increase of community-funded research projects and experimental campaigns focused on unfolding the complex and highly diverse behaviour of these process components. For example, the European research project INDUSE-2-SAFETY 2012-2015, investigated through experimental tests the performances of several NSCs and their limit state levels to be compliant with. Conversely, the United States Nuclear Regulatory Commission agency carried out a multi-year test programme to develop a better understanding of the elastoplastic response and ultimate strength of nuclear power piping systems. As a result, in view of the enhancement of structural integrity of industrial, energy and nuclear components as well as fitness for service, design guidelines and recommendations were issued (NISTGCR 2017).

Despite the available technical solutions, earthquakes remain one of the most harmful natural hazards in industrial plants due to domino effects. The applicability of conventional base isolation is limited to specific exceptional cases mainly because seismic isolation devices exhibit a limited life cycle time due to certain components -e.g. rubber bearings, friction surfaces, seals, etc.-. Recently, innovative scientific and technological concepts have been developed within the broad field of metamaterials (Maldovan 2013). These are natural or artificial materials or structures which exhibit extraordinary properties for inhibiting or conditioning wave propagation in all spatial directions over broad frequency bands. Such materials are already finding successful technological applications for high-frequency waves, i.e. electromagnetic, optical, thermal and ultrasound. Quite recently, the application of metamaterial concepts has also been proposed for seismic and sound waves (Palermo et al. 2016; Basone et al. 2019a; Miniaci et al. 2016; Hussein et al. 2014). These initial developments have further advanced through novel absorption and isolation concepts, such as the addition of negative effective mass and stiffness devices, and periodic structures endowed with nonlinear mechanisms, e.g. bistability (Frazier and Kochmann 2017; Hussein and Frazier 2013; Bursi et al. 2021a). In this way, the limitations of existing seismic and low-frequency isolation technologies can potentially be overcome, leading to highly-damped, low-maintenance and easily implemented designs based on locally resonant metabarriers and metastructures capable of shielding critical equipment of industrial facilities. Similarly, new devices like inerters and nonlinear impact-based energy sink devices (NES) have been recently used in metastructures for mass reduction and free vibration mitigation (Rothos and Vakakis 2009; Wenzel et al. 2020).

Along these lines, the author has tried to integrate and exploit the new capabilities offered by metamaterials and metastructures, i.e. metafoundations, to expand standard safety systems e.g. seismic isolation; see, in this respect, Fig. 6.1.

With reference to broad tanks subjected to seismic loading, instead, relevant fragility functions were determined by means of 3D FE models and low-fidelity

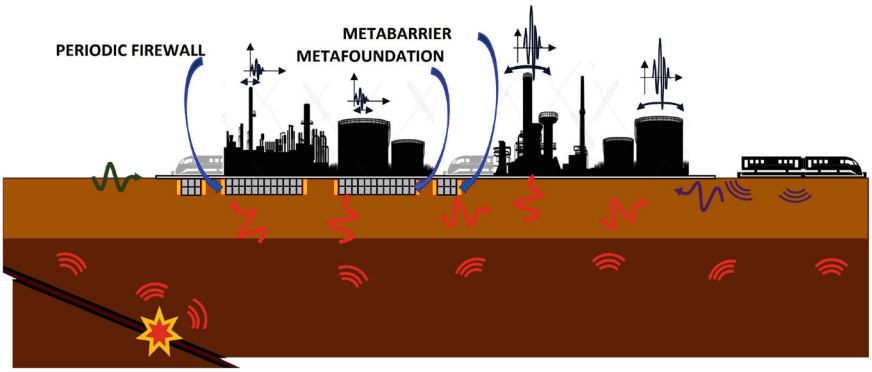

Fig. 6.1 Reduction of vibrations due to seismic loadings and other hazards through the use of metastructures in a petrochemical facility

kriging models based on Gaussian process regression (Phan et al. 2020) the stochastic nature of the input was taken into account. Finally, both aleatoric and epistemic uncertainties with their propagation in the design/modelling of metamaterials and metastructures still need to be examined in depth (Celli et al. 2019).

One of the important challenging points of utilizing MF is the excessive size necessary to obtain an operational design and the material strength and technology limitations to reach optimum stiffness and damping requirements. For the solution, many different approaches and techniques including nonlinearities and novel devices have been proposed. In the case of heavy or low-frequency superstructure, the resonators need to be tuned at ultra-low frequency ranges, which can be solved with the use of negative stiffness elements in parallel with the wire ropes that attach the resonators to the main cell (Wenzel et al. 2020). Bursi et al. (2021b) investigated the wire ropes in the nonlinear range using hysteretic Bouc-Wen model and proposed an optimization method. Achieving proper attenuation necessitates the installation of substantially heavy resonators. One alternative approach to achieve mass amplification is by incorporating inerter devices. Inerters respond with a force that is directly proportional to the relative acceleration between their two terminals (Smith 2002). The significant advantage of using inerters lies in their ability to possess inertance levels several orders of magnitude higher than the actual mass. As a result, the inertance term -b- does not factor into the equation of motion for the dynamic system under the influence of ground motion. In the field of structural engineering, many researchers have proposed the use of inerters to enhance seismic protection (Ma et al. 2021; Liu et al. 2022). Giaralis and colleagues conducted studies on Tuned Mass Dampers (TMDs) equipped with inerters, exploring their effectiveness in suppressing vibrations caused by both wind and earthquake excitations (Marian and Giaralis 2017; Giaralis and Petrini 2017).

6.1.2 Scope

The first part of this work presents an innovative, efficient and accurate framework for the evaluation of state-dependent fragility functions for critical industrial process components. The relevant vulnerability assessment is based on the integration of data derived from an intensive experimental campaign, accomplished within the European SERA SPIF project, with the computational potential obtained from advanced meta-modelling techniques. The value of this framework resides in the experimental data on which it is built. These are the outcome of the comprehensive experimental programme completed at the EUCENTRE laboratories in Pavia (I). More precisely, the tests were carried out on a shaking table of two archetypes of industrial systems full-scale steel substructures, equipped with NSCs such as tanks, cabinets, BFJs, and piping elements. In fact, experimental data fill the gap in terms of experimental evidence of tests conducted in a PBEE framework capable of taking into account the effects of NSCs-primary structure coupling as a whole. Therefore, an added value of this work lies in the performance evaluation and study of the complex interactions between NSCs and the primary structures through the development of different highly refined numerical models capable of capturing interaction effects. They are conceived to be more quick and inexpensive-to-run and able to capture the global behaviour of each coupled system. For the sake of brevity, we'll concentrate on the braced frame.

Moreover, this chapter presents a novel seismic protection method for industrial process components. This method is based on the core concept of locally resonant metastructures, specifically termed finite locally resonant metafoundations (MFs). The specific objectives pursued to achieve this goal include: (i) the identification of parameters of MFs and possible benefits of introducing nonlinear dynamics to MFs to enhance the performance; (ii) the investigation of more efficient strategies to model superstructures for optimization and design of MFs; (iii) to ensure code-compliant design for MFs and to develop efficient optimization strategies to determine optimal resonator parameters; (iv) the implementation of bistable columns in metafoundations to leverage advantageous features of bistability such as harmonic energy diffusion and adaptive bandgaps, and to assess their impact on the characteristics of finite lattices and periodic systems. In addition, we underline the scientific and technical feasibility of the proposed solutions. Finally, conclusions and future perspectives are drawn.

6.2 Dynamic Performance of a Multistorey BF Frame Structure with Process Equipment Subjected to Site-Based Ground Motion

The problem complexity and the inherent modelling of plants concur in limiting the development of risk assessment methods, such as component and system fragility, based on meaningful reduced and quick-to-run models. FE-based and surrogate models, such as Kriging, can then be used to estimate both component and system fragility functions of process equipment coupled to the primary structures.

6.2.1 A New Framework for System Vulnerability Assessment

Due to constraints in time and available information, risk-informed assessments are often conducted using simplified, quick-to-evaluate models. However, as emphasized in the recent NISTGCR 17-917-44 (NISTGCR 2017) report on industrial facilities, these established approaches do not result in economically viable or rational designs. Building on this, the current subection introduces the concept of a new framework for system vulnerability assessment. This framework leverages a combination of experimental data and surrogate models, facilitating the computation of state-dependent fragility curves that account for multiple aspects of the problem. State-dependent fragility curves are a specific type of fragility curve that are conditioned not only on a measure of seismic intensity (IM), which is typically represented as a vector, but also on the initial state of discrete damage (DSi) of the structure (see Iervolino et al. 2015b). These curves therefore allow for the evaluation of a system's vulnerability after it has already sustained damage, as defined by the generalized equation,

$$\begin{aligned}\mathbb{P}\Big[\mathrm{DS_j}|\mathrm{DS_i},\ \boldsymbol{IM}=\boldsymbol{im}\Big] &= \mathbb{P}\Big[\mathrm{DS}\geq \mathrm{DS_j}|\mathrm{DS_i},\ \boldsymbol{IM}=\boldsymbol{im}\Big]+\\ &-\mathbb{P}\Big[\mathrm{DS}\geq \mathrm{DS_{j+1}}|\mathrm{DS_i},\ \boldsymbol{IM}=\boldsymbol{im}\Big],\end{aligned} \tag{6.1}$$

for $j > i$, with i indices representing the identified damage limit states. Figure 6.2a illustrates the generalized transition probability state matrix for a system with three possible levels of damage -labeled DS0 to DS2-; whilst Fig. 6.2b depicts the associated Markovian diagram transition states.

As a consequence, the derivation of state-dependent fragility functions inherently lies in a vast number of Monte Carlo analyses. However, the complexity of the FE models hinders the direct derivation. Hence, an innovative UQ framework based on a reduced number of expensive FE simulations and on leveraging cutting-edge surrogate model techniques is proposed. Specifically, Fig. 6.3 outlines the UQ-based framework and the key steps for performing state-dependent fragility analysis. The top row, highlighted with a red contour, represents the brute-force MCS

Initial damage state DS_i \ Transition to damage state DS_i	$\mathbf{DS_0}$	$\mathbf{DS_1}$	$\mathbf{DS_2}$
$\mathbf{DS_0}$	$1 - \mathbb{P}_{01} - \mathbb{P}_{02}$	$\mathbb{P}[DS \geq DS_1 \mid DS_0, IM] - \mathbb{P}[DS \geq DS_2 \mid DS_0, IM]$	$\mathbb{P}[DS \geq DS_2 \mid DS_0, IM]$
$\mathbf{DS_1}$	×	$1 - \mathbb{P}_{12}$	$\mathbb{P}[DS \geq DS_2 \mid DS_1, IM]$
$\mathbf{DS_2}$	×	×	1

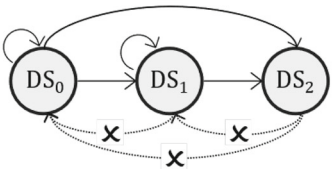

Fig. 6.2 Transition state: **a** matrix and **b** diagram, respectively

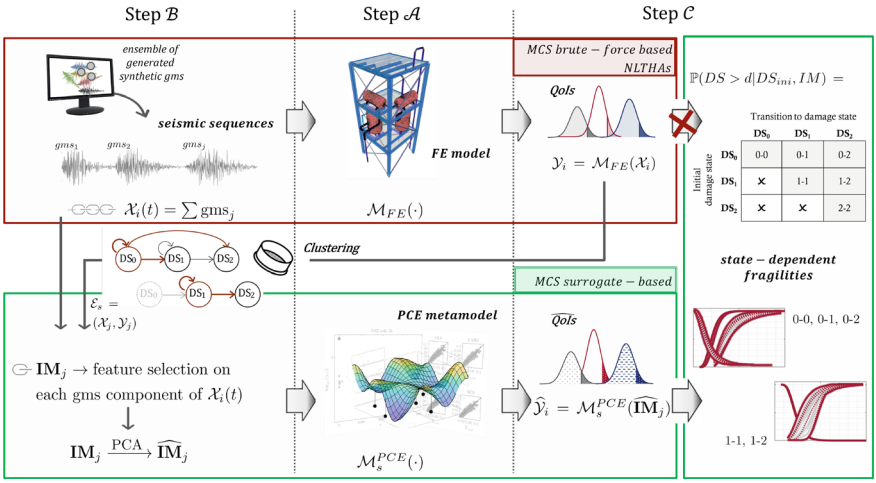

Fig. 6.3 UQ-based framework and key steps for performing a state-dependent fragility analysis

approach using computationally expensive NLTHAs (steps $\mathcal{A}$ to $\mathcal{C}$), whilst the green-highlighted row illustrates the surrogate-based MCS method. In the top row, step $\mathcal{A}$ involves developing complex and computationally intensive FE models, followed by step $\mathcal{B}$, where a ground motion model is used to generate stochastic seismic sequences as input. However, the heavy computational load limits the feasible number of MCS runs, creating a constraint on the derivation of state-dependent fragility functions, as indicated by the interrupted red-crossed arrow. Despite this, the limited NLTHA QoIs obtained are clustered based on the initial damage state metric DS0,1,2. These clustered data, along with the corresponding seismic event sequences, form the DoE Ds for the surrogate models (steps $\mathcal{A}$ and $\mathcal{B}$). First, a comprehensive vector of IMs

is extracted, and then a principal component analysis (PCA) is applied to reduce the input dimensionality. This reduction allows for the construction of polynomial chaos expansion (PCE) metamodels for each Ds, where s ∈ [DS0, DS1]. Finally, a large number of surrogate-based MCS runs are conducted, enabling the derivation of state-dependent fragilities (step $\mathcal{C}$).

6.3 Industrial Case: A Vertical Tank Installed on a Special-Risk 3D Braced Structure

The assessment of system fragility functions is herein presented for the industrial mock-up of the project SPIF #2, i.e., *Seismic Performance of Industrial Facilities*. Specifically, the project consisted of a comprehensive experimental shake table test campaign on an archetypal multi-component steel braced frame, endowed with industrial process components. A state-dependent fragility analysis was performed on one of the most critical equipment installed on the structure, i.e., the vertical tank at the first-floor level. The fragility analysis focused on this component, leveraging bootstrap-PCE and campaign data insights.

6.3.1 Step $\mathcal{A}$—Computational Model Description

6.3.2 Computational Models

FE physics-based model. The considered FE model represents the outcome of the recent SPIF #2 experimental research campaign, i.e. *Seismic Performance of Industrial Facilities*, performed by means of shaking table tests at EUCENTRE Laboratory, Italy. Figure 6.4a depicts the industrial substructure model tested on the shaking table. The mock-up consists of a full-scale 3-storey steel braced frame (BF) structure with flexible floors. Several NSCs of the industrial process were installed, like tanks, cabinets, bolted flange joints, and T-joints. Particularly, the complex dynamic interaction between the main steel structure and one of the NSCs—the vertical tanks mounted on the first level—was of great interest. The strong rocking exhibited by those components deserved attention due to the possible disastrous consequences related to damage on them. Figure 6.4a shows the investigated vertical tank. Careful notice was paid to the FE modelling. In this respect, Fig. 6.4b reports a detail of the ad-hoc designed stick model for the tanks and its expensive reference high-fidelity local FEM. The stick model was developed with the goal to: (i) mimic the modal properties and: (ii) catch the different effects of the participating seismic mass on the supporting girders system, varying with the intensity level of the seismic excitation. A thorough discussion on FE modelling and calibration of the global SPIF #2 model of Fig. 6.4c is deferred in Quinci et al. (2023). This was accomplished through the

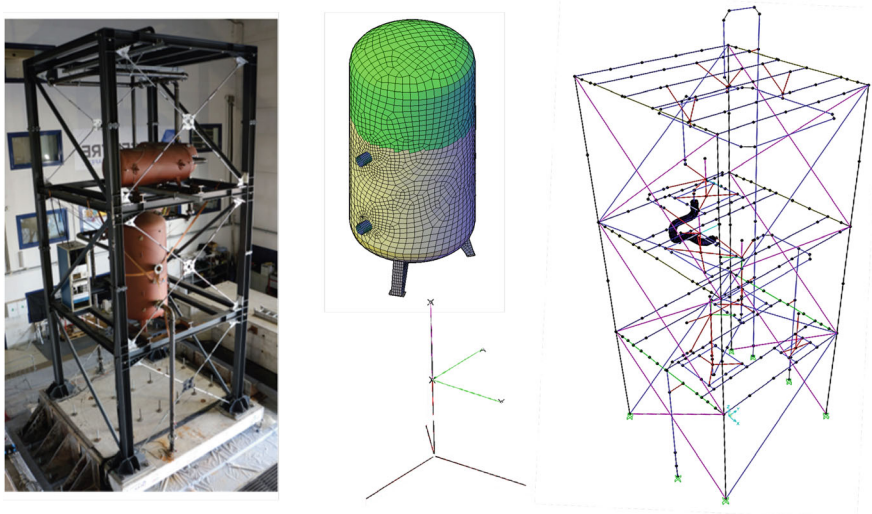

Fig. 6.4 The SPIF #2 mock-up: **a** photo of the braced frame (BF) configuration on the shake table of EUCENTRE Facilities and details of the vertical tank installed at the first level; **b** SAP2000®high-fidelity local FEM and ad-hoc implemented stick-model for the vertical tank; **c** global SAP2000®FEM of SPIF #2

deployment of complex and time-consuming high-fidelity local FE models, which were then used to assemble and calibrate the global physics-informed FE model in Fig. 6.4b.

The shake table tests showed that among the installed components, the vertical tanks were found to be critical and of greater interest. Therefore, fragility analysis is focused on these elements, leveraging bootstrap-PCE and campaign data insights.

6.3.3 Step 𝔅—Input Definition

To simulate different damage initial configurations and cover each transition state, sequences of seismic events were assigned as input to the NLTHAs of the FEM of SPIF #2. A total of 100 gms sequences, consisting of chains of 5 earthquakes each, were cast by the same ensemble of gms generated by the stochastic ground motion model of Rezaeian and Der Kiureghian (2010). The computational cost pro single sequential NLTHA is ∼30 min on an Intel(R) Core(TM) i9-10900K CPU @3.70GHz, 10 Core(s)—128 GB RAM. Both the number of gms in a single sequence and the total number of sequential NLTHAs were determined by a trade-off between the total time required for analysis and a well-defined population of the transition matrix of Fig. 6.2b. The transition matrix for the vertical tank was defined on two performance

limit states. Those were inferred by the literature review, see Vathi et al. (2017), and confirmed by the experimental campaign, see Nardin et al. (2022). The first was the Design Basis Earthquake (DBE), which is linked to the operation and functionality of the process plant. The second was the Safe Shutdown Earthquake (SSE) limit state, for which the fundamental safety functions can be ensured, although the facility is no longer operational. Thresholds were experimentally identified in Nardin et al. (2022) as maximum acceleration recorded at the base of the tank: 6.72 m/s^2 for DBE and 18.5 m/s^2 for SSE, respectively.

6.3.4 Step C—QoI Response

NLTHAs and experimental design generation. The results of the NLTHAs performed on the FE model were clustered into the identified six transition states of Fig. 6.2a. Specifically, DS_0 indicates the dataset associated with pristine initial damage conditions, whilst DS_1 denotes the dataset for which the threshold associated with the DBE limit state was exceeded. Lastly, DS_2 collects the results of simulations for which the SSE limit state was attained. Almost 47% of the simulations belong to the DS_0 damage state initial condition. Particularly, 13 and 7% transitioned from undamaged initial conditions to exceeding the DBE and SSE threshold at the end of the NLTHAs, respectively. Instead, 38% of simulations belong to DS_1, out of which 16% stayed in the same damage level even after other seismic shocks. Finally, 15% of the simulations reached the absorption state. Finally, in agreement with Table 6.1, 41 IMs were evaluated for each gms of the NLTHA simulations. To reduce the order of the input dimension, PCA was then applied to each gms. To achieve 99% of the variability of data, 10 PCs were needed.

PCE metamodelling. State-dependent fragilities required many more analyses than the ones performed on the expensive-to-run FE model. Hence, two metamodels were implemented to overcome the computational and time issues. Specifically, the first metamodel was built on the experimental design $\mathcal{E}_0$ of simulations belonging to the DS_0 dataset, i.e. with undamaged initial conditions. The second had as experimental design $\mathcal{E}_1$, the family of simulations belonging to DS_1, i.e., with damage initial conditions attaining the DBE limit state. Resampling with substitution was used on both the experimental design $\mathcal{E}_{0,1}$, thus generating sets of bootstrap replications. Due to the finite size of the experimental design, such sets of responses were deployed to calculate the statistics of interest, i.e., the quantiles of the PCE predictor. Hence, bootstrap PCE (bPCE) was carried out with a q-norm truncation with $q = 0.50$, maximum allowed interaction $r = 2$ and a number of replications $B = 500$. Based on the performance of the ε_{LOO} and εemp errors, the subspace pursuit (SP) solver performed best, as in the benchmark test. As a result, Fig. 6.5a reports the histogram of the surrogate predictor over the histogram distribution of the $\mathcal{E}_0$. The limit state thresholds of DBE and SSE are also reported. A favourable performance is attained, with a final ε_{LOO} error estimate of 4.17E-02. The estimation of bPCE coefficients

Table 6.1 A comprehensive list of ground motion IM parameters (De Biasio et al. 2015; Hariri-Ardebili and Saouma 2016

No.	Description of IM	Symbol	Mathematical model
1	Peak ground acceleration	PGA	$\max(\lvert\ddot{u}(t)\rvert)$
2	Peak ground velocity	PGV	$\max(\lvert\dot{u}(t)\rvert)$
3	Peak ground displacement	PGD	$\max(\lvert u(t)\rvert)$
4,..,8	Spectral displacement	Sd	$S_d(T_x)$
9,..,13	Spectral velocity	Sv	$S_v(T_x)$
14,..,18	Spectral acceleration	Sa	$S_a(T_x)$
* *where* T^* $\in$ [0.50; 0.35; 0.25; 0.15; 0.10]			
19	Arias intesity	I_A	$\pi/2g \cdot \int_0^{t_f} a^2(t)\mathrm{d}T$
20	Total cumulative energy	E_{cum}	$\int \ddot{u}^2(t)\mathrm{d}t$
21	Riddell–Garcia intensity acceleration	$I_{RG,a}$	$(PGA)^{+1} \cdot (T_d)^{+1/3}$
22	Riddell–Garcia intensity velocity	$I_{RG,v}$	$(PGV)^{+2/3} \cdot (T_d)^{+1/3}$
23	Significant time duration	T_d	$t_{95} - t_{05}$
24	Root mean square of acceleration	RMS($\ddot{u}$ (t))	$\sqrt{(\frac{1}{N}\sum_{n=1}^{N} \lvert x_N^2\rvert)}$
25	Characteristic intensity	IC	$\mathrm{RMS}(\ddot{u}(t))^{1.5} \cdot T_d^{0.5}$
26	Cumulative absolute velocity	CAV	$\int_0^{t_f} \lvert a(t)\rvert \mathrm{d}T$
27	Cosenza–Manfredi intensity	I_{CM}	$2g/\pi \cdot (PGA)^{-1}(PGV)^{-1}(AI)^{+1}$
28	Average spectral acceleration	ASA_{40}	$2.5/f_1 \int_{0.6 \cdot f_1}^{f_1} S_a(f,\varepsilon)\mathrm{d}f$
29	Acceleration spectral intensity	ASI	$\int_{0.1}^{0.5} S_a(T,\varepsilon)\mathrm{d}T$
30	Effective peak acceleration	EPA	$1/2.5 \int_{0.1}^{2.5} S_a(T,\varepsilon)\mathrm{d}T$
31	Velocity to acceleration ratio	$I_{v/a}$	PGV/PGA
32	Fajfar intensity	I_F	$(PGV)^{+1} \cdot (T_d)^{+1/4}$
33	Mean frequency	F_m	$\sum_i U_i^2(f_i)/\sum_i U_i^2$
34	Rate of change mean frequency	$\dot{F}_m$	$\mathrm{d}F_m(T)/\mathrm{d}t$
35	Fourier amplitude spectrum area	FAS_{area}	$\frac{1}{4df}\int_{f_1-2df}^{f_1+2df} U(f)\mathrm{d}f$
36,..,41	Equipment relative average spectral acceleration	$E - ASA_{R_x x}^{**}$	$\frac{1}{f_1 \cdot (X_f - 1)} \cdot \int_{f_1}^{X_f \cdot f_1} S_a(f,\varepsilon)\mathrm{d}f$

** R indicates the chosen percentage of drop of the fundamental frequency ($X_f = 1 - (R/100)$); $R \in$ [40; 67; 80; 100; 150; 200]

converged to a polynomial degree order of 3. Moreover, Fig. 6.5b shows the control $Y_{\mathcal{E}_0} - Y_{bPCE}$ plot: a good alignment is found with the 45° line, which represents the ideally perfect match between true and surrogate data.

Similarly, bPCE was performed for the experimental design $\mathcal{E}_1$. Anew, a q-norm truncation with $q = 0.50$, maximum allowed the interaction $r = 2$ and a number of replications $B = 500$ was applied. According to the εemp error, the SP solver was identified as the best one. However, the optimal matching pursuit OMP solver also performed significantly well regarding the εLOO error. As a result, Fig. 6.6a reports

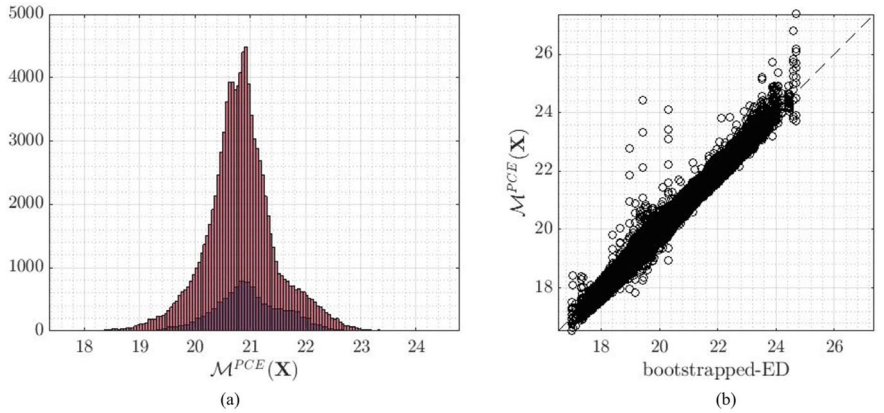

Fig. 6.5 **a** Histogram distribution of the PCE surrogate Y_{PCE} (light gray) predictor *vs* the $Y_{\mathcal{E}_0}$ original data of the initial undamaged condition dataset; **b** control plot of the performance of the Y_{bPCE} surrogate model *vs* the $Y_{\mathcal{E}_0}$ reference experimental design samples

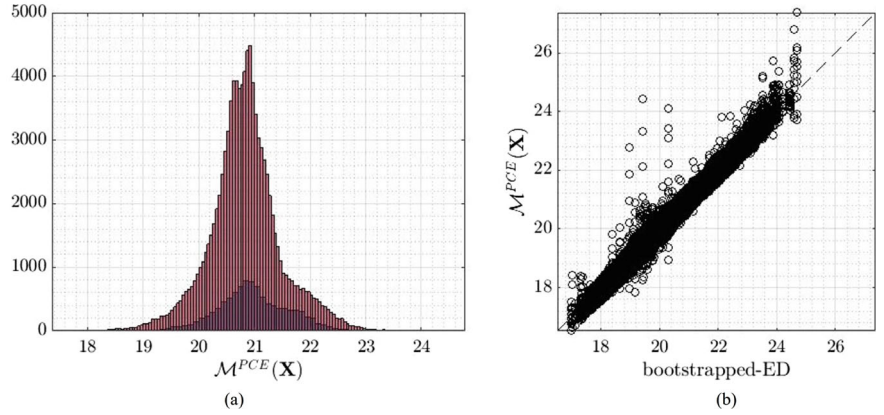

Fig. 6.6 **a** Histogram distribution of the PCE surrogate Y_{PCE} (light gray) predictor *vs* the $Y_{\mathcal{E}_1}$ original data of the initial undamaged condition dataset; **b** control plot of the performance of the Y_{bPCE} surrogate model *vs* the $Y_{\mathcal{E}_1}$ reference experimental design samples

the histogram distribution of both the Y_{PCE} predictor and the $Y_{\mathcal{E}_1}$ data of the damaged initial state condition. A generally good agreement is found, with a few exceptions in the range between [21 and 22] m/s^2. This is reflected also in the control plot Y_{bPCE}–$Y_{\mathcal{E}_1}$ of Fig. 6.6b, where the dispersion is greater in that range. The estimation of PCE coefficients converged at a polynomial degree of order 5 with a final ε_{LOO} error of 4.73E-02.

Fragility assessment. To determine which IM is better, the efficiency index β_{eff} is evaluated for each transition state. Particularly, the optimal IM correspond to the

one whereby the variability of the EDP is minimal. Consequently, for each IM, the efficiency index β_{eff} was evaluated as follows:

$$\beta_{\text{eff}}(im) = \min\mathbb{E}\left(\text{IQR}|_{im,x_1} + \text{IQR}|_{im,x_2} + \text{IQR}|_{im,x_3}\right) \tag{6.2}$$

where IQR stands for the 90th inter-quantile range evaluated in correspondence of the 25th–50th–75th quantile of the IM axes. The lower the β_{eff} index, the better the performance of the IM. Specifically, the PGA, E_{cum}, and $\text{E} - \text{ASA}_{\text{R67}}$ are the optimal IM that occurred more often. Those are positively correlated with acceleration and energy content; see, in this respect, the definition reported in Table 6.1; whilst, another IM that often recurred, was the I_{F}, correlated with velocity terms. As thoroughly investigated in the research paper (Fajfar et al. 1990), the I_{F} captures damage for structures with fundamental periods in the medium-period (velocity-controlled) region. Instead, the $\text{E} - \text{ASA}_{\text{R}_{67}}$ IM captures the presence of significant spectral acceleration ordinates over the structure's dominant frequency interval, as reported in De Biasio et al. (2015). Therefore, it accounts for damage by detecting frequency shifts due to structure-component coupling effects. These observations agree with the experimental evidence described in Nardin et al. (2022). More precisely, the processing of the collected data revealed a significant correlation between the maximum floor spectral acceleration $Sa_{floor}(T_{NSC})$, evaluated at the identified period $T \simeq 0.16$s of the vertical tanks and the $\text{E} - \text{ASA}_{\text{R}}$ measure.

Figure 6.7 reports the state-dependent fragility curves as functions of the PGA. In the Fig. 6.7, dark-red lines and the associated shaded areas highlight the 50, 90 and 99% confidence bounds, respectively. Given an initial damage condition, i.e., -graphically- for elements of the same row, the variability increases towards higher damage states, i.e., moving to the right. Similarly, given a damage limit state to attain, i.e., -graphically- for elements of the same column, the required magnitude of IM to reach the same exceedance probability is lower. For instance, the 50% probability of exceedance DS_2 given DS_1 and DS_0 is associated to PGA = 2 and PGA = 3.7 m/s^2, respectively.

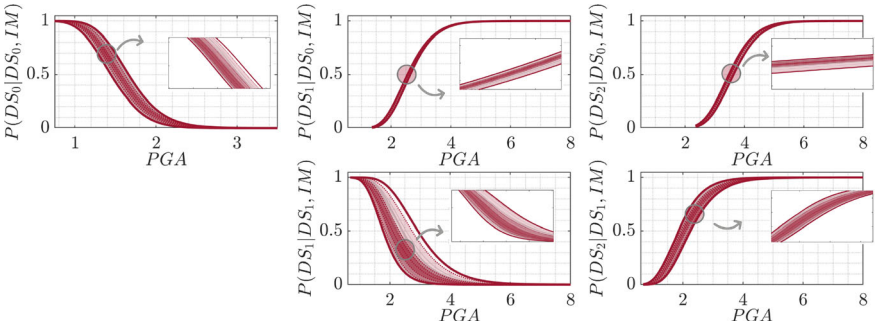

Fig. 6.7 Bootstrapped-PCE state-dependent fragility curves of the SPIF #2 vertical tank with PGA as IM: dark-red thick lines stand for the 50, 90 and 99% confidence bound, along with lighter to darker shaded areas

6.4 Numerical and Experimental Activities on Bistable Components and Metamaterials

6.4.1 Numerical Characterization of Bistable Systems

Bistable oscillations have garnered significant attention in the last decade due to their sophisticated and diverse dynamics. Bistability is characterized by a system with two stable equilibrium states, and is observed in biological systems like genetics (Dubnau and Losick 2006) and neuroscience (Knapen et al. 2011; Durstewitz and Seamans 2006). In the mechanical field, buckled columns or beams serve as examples of bistable systems (Cazottes et al. 2009). Therefore, the advantages of bistable oscillations have entailed wide applications in various phenomena, including energy harvesters (Harne and Wang 2013; Arrieta et al. 2010), nonlinear energy sinks (Habib and Romeo 2017), and MEMS (Saif 2000).

Bistable systems exhibit a complex feature known as stochastic resonance (Gammaitoni et al. 1989), characterized by snap-through dynamics induced by low-level noise and periodic excitation. Interestingly, individually, both low-level noise and periodic excitation are insufficient to trigger interwell dynamics (snap-through motions between two stable configuration), making bistable systems beneficial for energy harvesting. Furthermore, the presence of strong nonlinearity in these systems leads to chaotic responses, as per chaos theory, revealing underlying patterns and deterministic laws within the randomness of chaotic dynamics (Hopf et al. 1982). The butterfly effect (Lorenz 2000), characterized by extreme sensitivity to initial conditions, creates diverse and intricate dynamic response characteristics in systems enodwed with bistability.

The basic static nonlinearity exhbited by a bistable component can be obtained through a Duffing oscillator with a negative first-order and a positive third-order spring constants. In particular, the static force-deformation and potential energy relationships of a bistable Duffing oscillator with ($P_1 < 0$, $P_3 > 0$), is given in Fig. 6.8, where the positive and negative stiffness regions can be clearly identified. In the energy graph, the two stable points, the so called stable wells can be observed, and the distance between the cells corresponds to $\sqrt{|P_1/P_3|}$.

At the stable points, the Duffing spring is characterized by a stiffness value,

$$\left(P_1 x + P_3 x^3\right) \frac{d}{dx}\bigg|_{x=\pm\sqrt{-P_1/P_3}} = -2P_1 \tag{6.3}$$

whilst between the stable wells, the system exhibits softening, until reaching the negative stiffness region where the maximum absolute value of the negative stiffness will be reached at the unstable point, i.e. $x = 0$; at this point, the stiffness value reads P_1. When the dynamics are considered, in the most general terms the motion of the system can be divided into two parts: the intrawell motion and the interwell motion. In Fig. 6.9a in particular, the intrawell motion is given together with the phase portrait where the energy of the system is not sufficient to breach over the unstable point

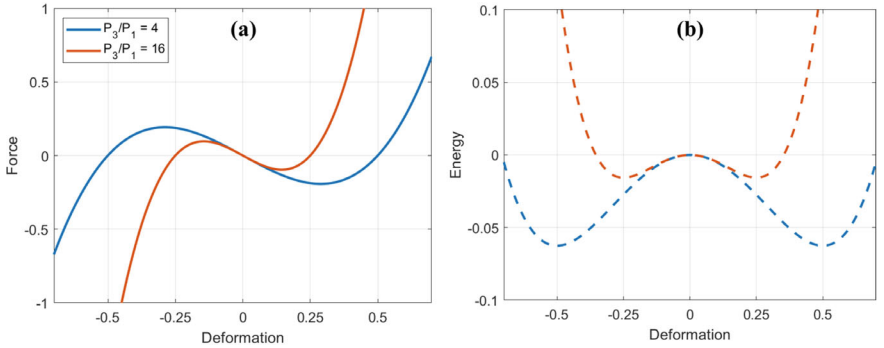

Fig. 6.8 Bistable Duffing oscillators: **a** force-deformation relationships; and **b** Relevant potential energies

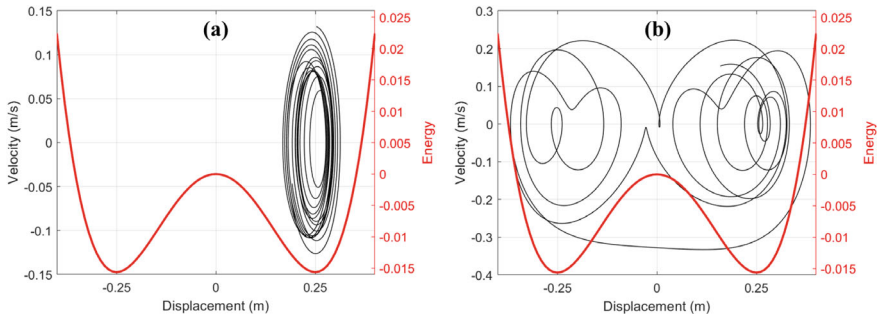

Fig. 6.9 Bistable Duffing oscillator motions in phase portrait: **a** Intrawell motion; and **b** Interwell motion

energy and the system oscillates around one of the stable wells. In Fig. 6.9b instead, the system has sufficient energy to overcome the potential peak in the middle; then, interwell motions can be observed, where oscillations happen between and around wells. These motions can also be distinguished according to their amplitude in small and large amplitude.

A bistable lattice composed of bistable undamped springs and masses is depicted in Fig. 6.10, and the EoM of the system can be written as,

$$m_n\ddot{x}_n + P_1(2x_n - x_{n-1} - x_{n+1}) + P_3(x_n - x_{n-1})^3 + \ldots \\ \ldots + P_3(x_n - x_{n+1})^3 = 0 \quad (6.4)$$

where $P_1 < 0$, $P_3 > 0$. Herein, it must be noted that the harmonic balance method (HBM) is not suitable for systems with aperiodic responses; as a result, an analytical solution was not pursued. The plot of the numerically obtained dispersion results are presented in Fig. 6.10 with various amplitudes. In the vicinity of dissipation and

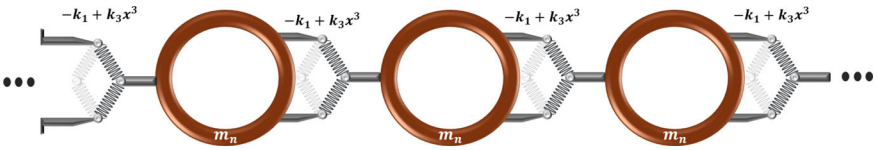

Fig. 6.10 A bistable periodic lattice

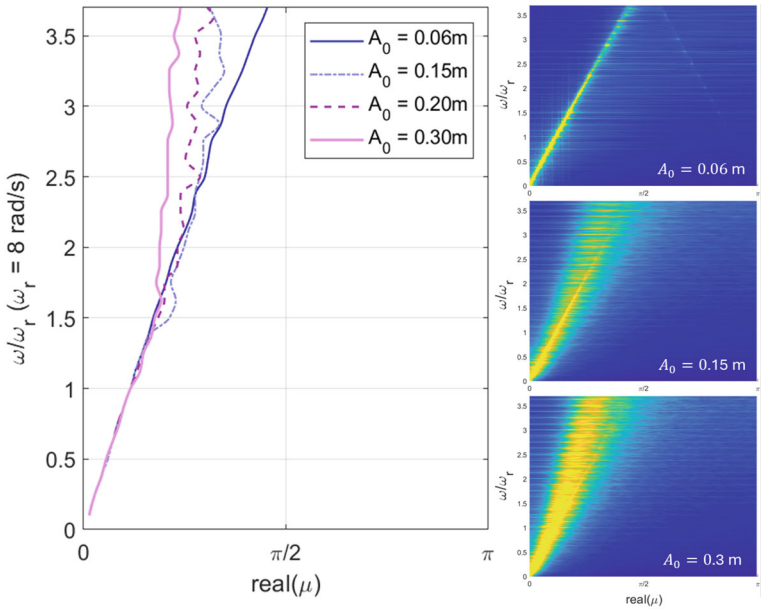

Fig. 6.11 Numerical dispersion bands for a bistable periodic lattice and relevant 2D FFT results

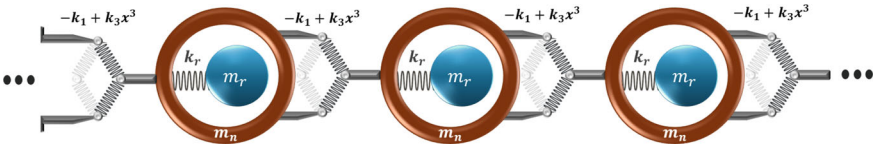

Fig. 6.12 Nonlinear LRM with the bistabity in the main cell springs

resonators, the propagation is continuous through the frequency range. One important aspect is the diffusion of wave propagation peaks, as amplitude increases, similarly to monostable Duffing cases (Fig. 6.11).

Furthermore, the bistablity can be introduced into the main cell springs of the LRM, as presented in Fig. 6.12. Herein, the aim is to extend the harmonic diffusion property of bistable springs to resonators, i.e. diffuse the anti-resonance property to multiple frequencies, thus providing a wider band gap. The numerical analyses

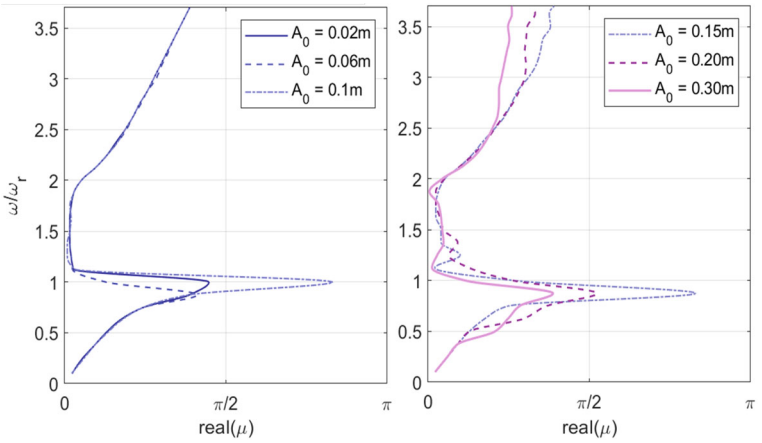

Fig. 6.13 Numerical dispersion results for LRM with bistable main cell springs

were conducted and dispersion relations were obtained for various amplitudes and are presented in Fig. 6.13.

6.4.2 Experimental Validation

Trough the fused deposition modelling (FDM), 3D-printed small-scale unit cells where printed, as illustrated in Fig. 6.14. To realize ultra-low frequency bistable LR finite metamaterials, the unit cells were considered as main cells; the main cell represents the outer mass depicted in Fig. 6.14 and connects to a resonator. Meanwhile, each resonators is only connected to the main frame with flexible linear elastic beams working in simple shear. Main cells connects to other main cells by means of slender beams working in shear too. To exhibit bistability, beams connecting every two main cells were designed to be on the onset of buckling under a preset axial load. The main cells were connected to each other and to the shake table either by linear or bistable beams as depicted in Fig. 6.14. More specifically, the distance between the main cells is 100 mm; then, 100 mm beams for the linear case and 116 mm beams for the bistable case were used. Since beams are considered to bend in shear, slender rectangular beams were considered to prevent yielding.

Apart from beams, all parts were 3D printed with ABS material. This provided sufficient stiffness and durability, as ABS is characterized by high toughness and resistance. In the case of bistable beams, the ABS was preferred since stress localization were not observed. In addition, the TPU material was used to reach lower resonance frequency for the resonator beams. The Cubic infill at 20% was considered for the ABS parts whilst beams were printed with 100% infill.

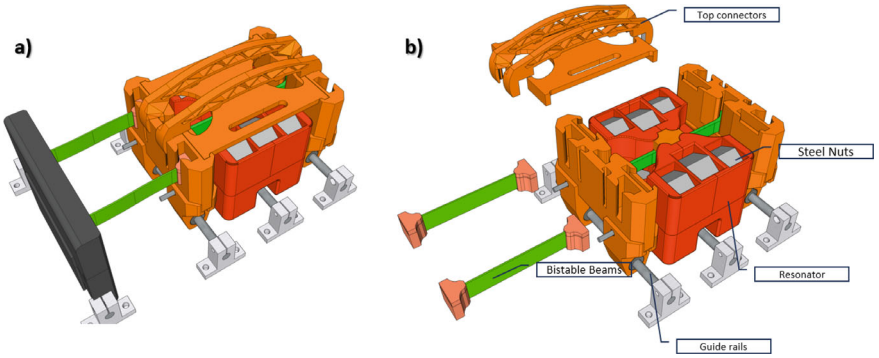

Fig. 6.14 A 3D printed bistable unit cell with the nonlinearity concentrated in the beams: a) the whole system including the resonator; b) the exploded view

The shear stiffness of the beams and the elastic modulus of the materials were determined through displacement-controlled static tests, as depicted in Fig. 6.15. As a result, the elastic modulus of the beams read 1.36 ± 0.15 GPa, whilst the shear stiffness of a linear beam was estimated to be 325 ± 20 N/m. Additionally, the masses of the main cell parts and the resonator were estimated to be 280 and 620 g, respectively. To increase the resonator mass, steel blocks were inserted into pre-designed holes, as indicated in Fig. 6.14b. Accordingly, the frequency of a unit cell without a resonator, was estimated to be 5.9 ± 0.2 Hz, and the resonator frequency was estimated to be 4.5 Hz.

A shake table is illustrated in Fig. 6.16; it is endowed with 500×500 mm and was utilized to provide a dynamic input. It is a TDG Desktop Shake Table v2, and is capable of delivering excitations in the range, 1–2 g, with a payload of 100–50 kg, respectively. It can achieve a maximum velocity of 500 mm/s.

The initial set of tests involved a single linear unit cell with and without a resonator subjected to a frequency sweep excitation, between 1 and 10 Hz. Displacement responses were measured through a laser vibrometer and high speed digital image correlation system. Using the FFT, the frequency content of the response was calculated and compared with the expected frequency responses obtained from accelerometer measurements; see, in this respect, Fig. 6.17. Due to frictional forces, the results revealed a slight increase in the resonant frequencies, i.e. 6.2 Hz.

To identify damping properties including Coulomb and viscous damping, as well as the parameters of the resonator, two types of frequency sweeps were conducted. These sweeps, featuring amplitudes of 5 and 8 mm, respectively, extended up to 10 and 8 Hz. The tests were performed on a single unit cell connected to the shake table using linear beams, both with and without resonator. Consequently, four tests were conducted, during which displacement data from both the shake table and the main frame were recorded. The identification was conducted considering the following system of EoMs:

$$\mathbf{M}\ddot{x} + \mathbf{C}\dot{x} + \mathbf{F}_f(\dot{x}) + \mathbf{F}_k(x) = \mathbf{F}_{ext}(\omega, t) \tag{6.5}$$

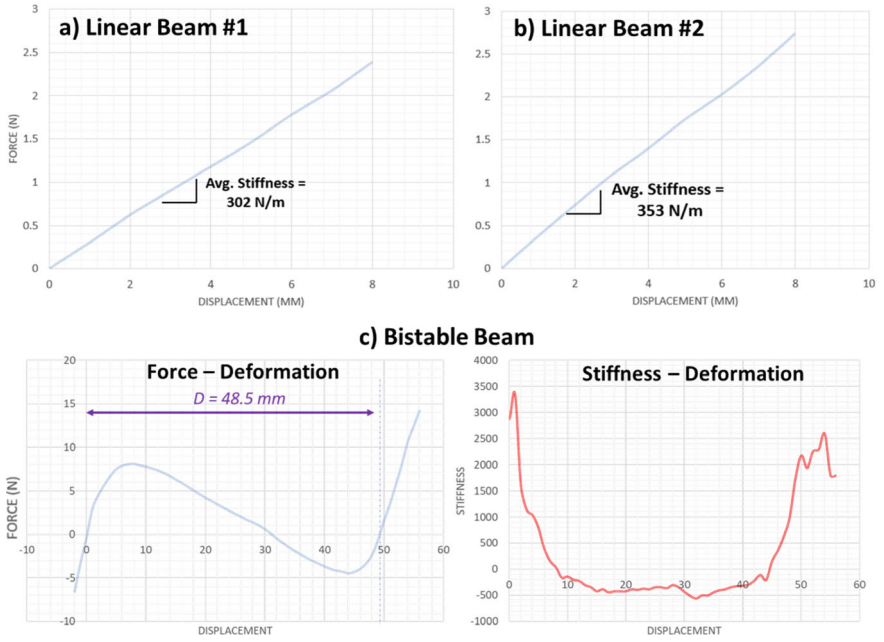

Fig. 6.15 Static identification of linear and nonlinear (bistable beams): **a** Positive stiffness of linear beam #1; **b** Positive stiffness of linear beam #2; and **c** Bistable beam response

where $\mathbf{C} = \mathbf{C_0} + \mathbf{C_1}\dot{x}$. For a bistable LRM lattice with single cell, the matrices of (6.5) can be expanded as follows:

$$\mathbf{M} = \begin{bmatrix} m_m & 0 \\ 0 & m_r \end{bmatrix} \tag{6.6}$$

$$\mathbf{C}_0 = \begin{bmatrix} c_{m,0} & -c_{r,0} \\ -c_{r,0} & c_{r,0} \end{bmatrix} C_1 = \begin{bmatrix} c_{m,1} & -c_{r,1} \\ -c_{r,1} & c_{r,1} \end{bmatrix} \cdot \dot{x}$$

$$\mathbf{F}_f = \begin{bmatrix} F_{f,m}(x) & -F_{f,r} \\ -F_{f,r} & F_{f,r} \end{bmatrix} \tag{6.7}$$

$$\mathbf{F}_k = \begin{bmatrix} f_k(x) & -k_r \\ -k_r & k_r \end{bmatrix} \tag{6.8}$$

where subscripts m and r represents the main cell and resonator, respectively. The stiffness term, $f_k(x) = k_1 x + k_3 x^3$, is a cubic polynomial used for the bistable beam, whilst $k_3 = 0$ for a linear beam. For ease of integration, the dry friction term, F_f was expanded following the formulation presented in Specker et al. (2014) and summarised as follows,

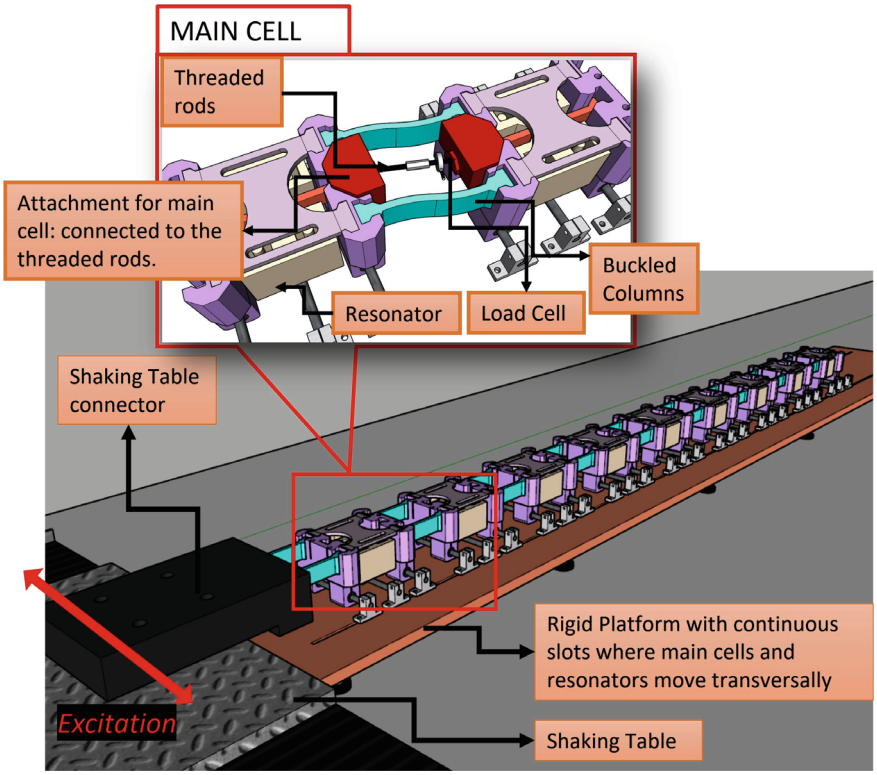

Fig. 6.16 A chain of 3D FFF printed nine bistable unit cells connected to the TDG Desktop Shake Table v2

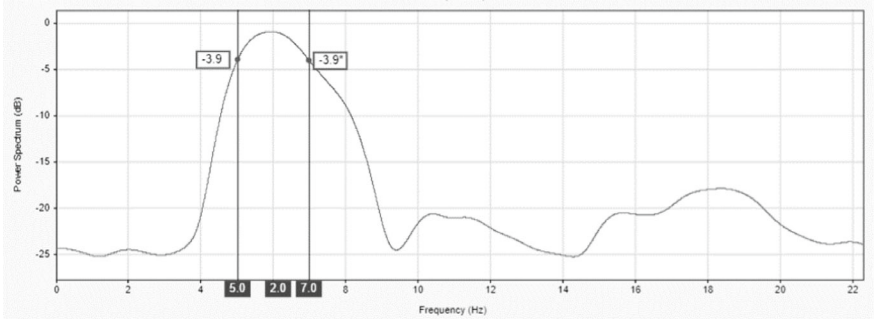

Fig. 6.17 FFT of an accelerogram obtained from MPU6050 on the top connector; see Fig. 6.14

$$F_f = F_{st} + F_{kin}\left(\tanh(\dot{x}/\dot{x}_{vt}) - g_f\right) \tag{6.9}$$

$$g_f = \frac{\dot{x}}{\dot{x}_{sp}} e^{\left(0.5-\left(\frac{\dot{x}}{\sqrt{2}\dot{x}_{sp}}\right)^2\right)} \tag{6.10}$$

where F_{st} and F_{kin} define the static and kinetic friction terms. Accordingly, the proposed numerical model requires a total of 13 parameter to be identified: (i) stiffnesses, k_1, k_3, k_r ; (ii) viscous damping constants, $c_{m,0}, c_{m,1}, c_{r,0}, c_{r,0}$; (iii) static and kinetic friction forces, $F_{s,m}$, $F_{k,m}$, $F_{s,r}$, $F_{k,r}$; and (iv) the Stribeck peak, and the kinetic friction velocity terms, $\dot{x}_{sp}, \dot{x}_{vt}$. To determine these 12 parameters, the numerical model of the unit cell was subjected to a driven boundary input, utilizing input histories recorded from shake table tags. By applying the Newmark method, the numerical response of the unit cell was obtained. The parameters were then determined through the minimization of the experimental FRFs and numerical FRFs, within a multi-variate optimization problem solved by a Genetic Algorithm. The optimized values, i.e. identified parameters, are collected in Table 6.2, whilst the FRFs comparisons are depicted in Figs. 6.18 and 6.19.

Table 6.2 Identified parameters

	k_1 (N/m)	k_3 (N/m^3)	c_0 (Ns/m)	c_1 Ns^2/m^2	$F_{f,s}$ (N)	$F_{f,k}$ (N)
L. Mc.*	441.8	–	1.30	6.7	1.4	0.76
B. Mc.*	1135.7	2.15e6	1.30	6.7	1.4	0.76
Res.*	552.3	–	0.96	14.9	9.2	0.45

* L.Mc.: Linear Main Cell, B.Mc.: Bistable Main Cell, Res.: Resonator

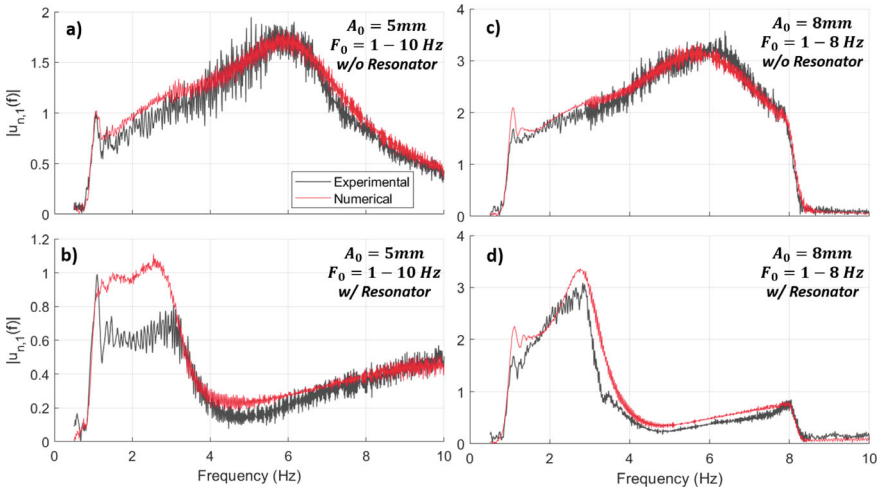

Fig. 6.18 The FRFs comparison between numerical and experimental results evaluated on a linear unit cell

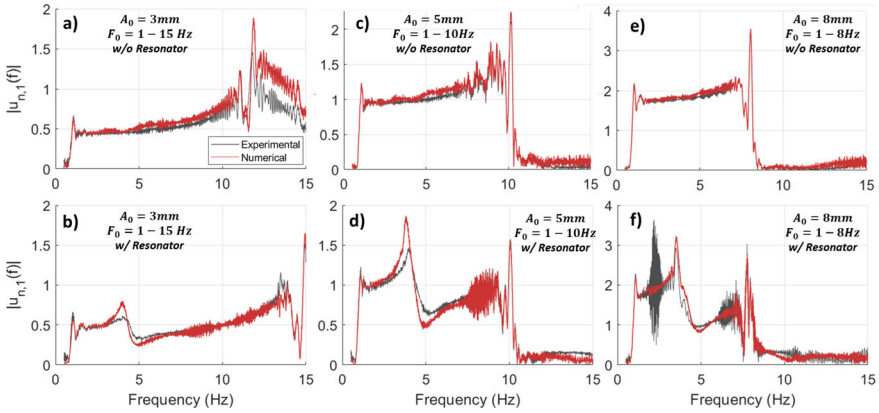

Fig. 6.19 The FRF comparison between numerical and experimental results for bistable unit cells

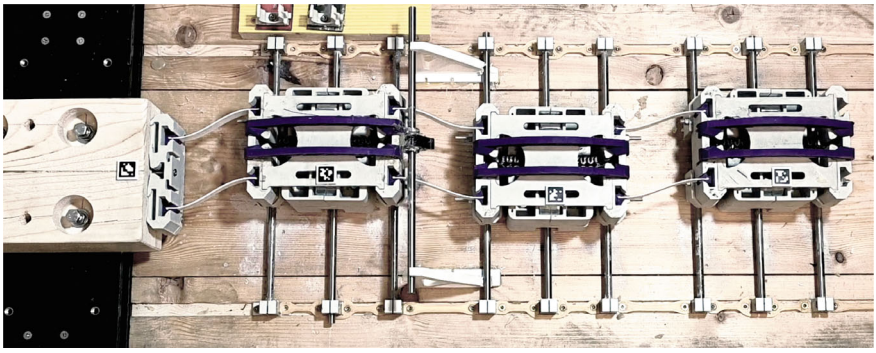

Fig. 6.20 Finite lattice with 3 bistable unit cells

Following the primary objective of bistable LRMs, the subsequent results present experimental findings regarding wave attenuation characteristics. In essence, chains consisting of single and three linear and bistable unit cells were subjected to both frequency sweep and sinusoidal inputs. The setup for the three-cell configuration is illustrated in Fig. 6.20.

Displacement time history results of single linear and bistable unit cells subjected to frequency sweep are presented in Figs. 6.21 and 6.22, respectively. Unit cells were tested both with and without resonator attached. The effect of the resonator can be seen in both cases where significant wave attenuations are achieved.

Since bistable oscillators have an offset stable point, a better comparison can be made in the velocity domain. Accordingly, the velocity FRFs are shown in Fig. 6.23. The presented cases show the benefits of resonators rather than a direct performance comparison between linear and bistable cases. Since bistable LRM exhibit wide range of dynamics, a more comprehensive investigation is necessary for direct comparison between linear and bistable cases.

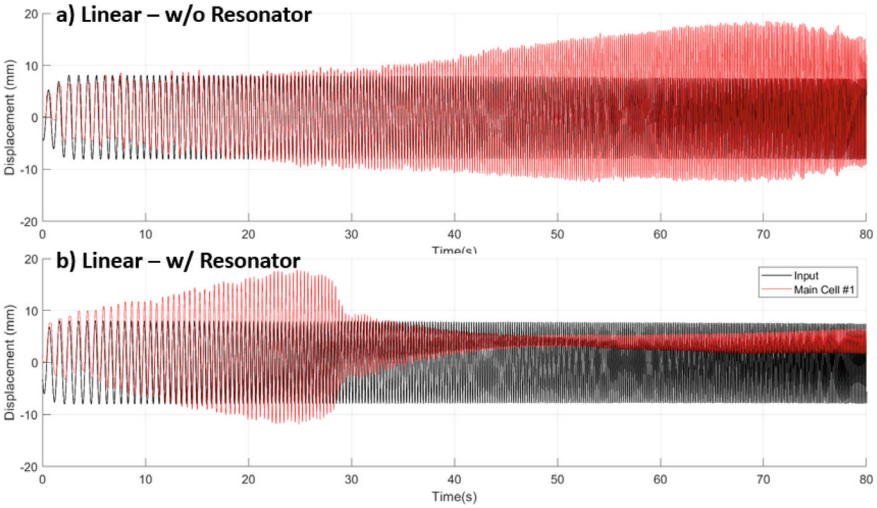

Fig. 6.21 Single linear unit cells with and without resonator subjected to a frequency sweep (8 mm, 1–8 Hz)

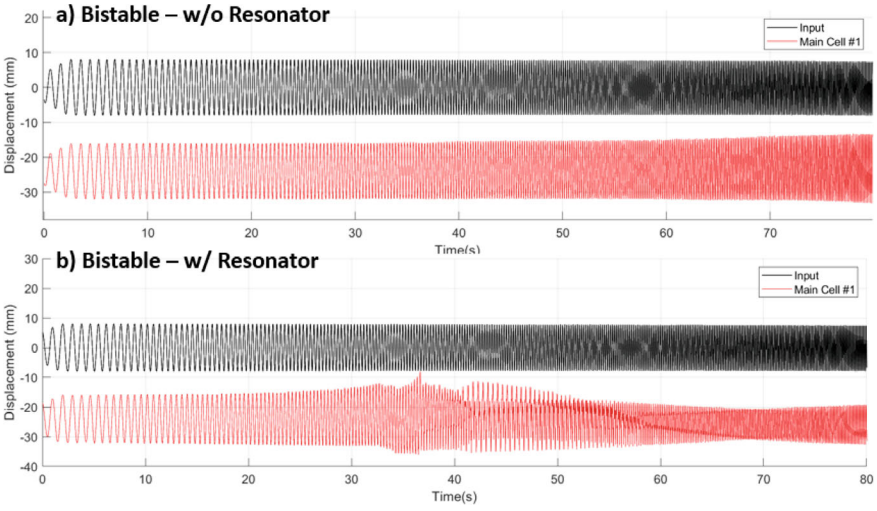

Fig. 6.22 Single bistable unit cell with and without resonator subjected to a frequency sweep (8 mm, 1–8 Hz)

Considering the triple unit cell setup, provided in Fig. 6.20, the velocity FRFs considering a frequency sweep at 8 mm amplitude are presented in Fig. 6.24 for the bistable LRMs. When a resonator is attached and despite the fact that it is not tuned for high frequencies, it can be observed that the a bistable LRM prevents the high frequency content to be transmitted to the last cell of the chain.

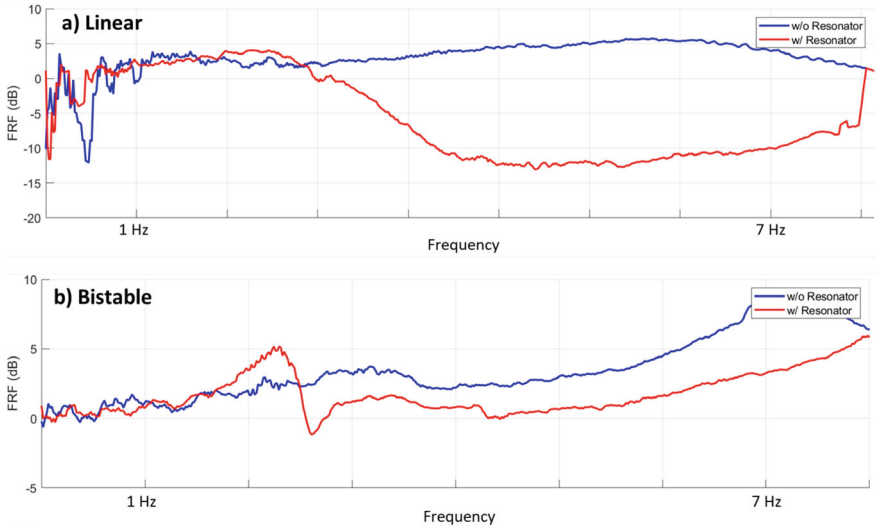

Fig. 6.23 Velocity FRF of Single unit cell with and without resonator subjected to frequency sweep (8 mm, 1–8 Hz)

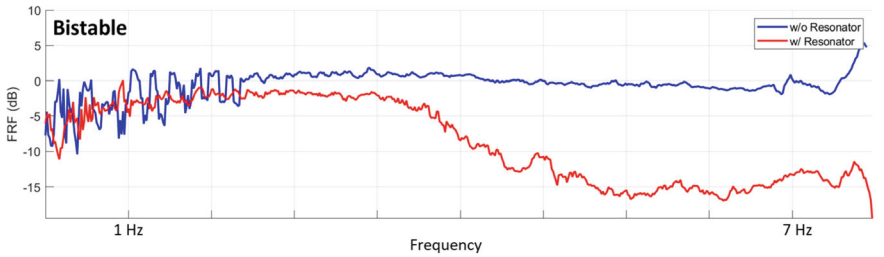

Fig. 6.24 Velocity FRF of a triple cell bistable LRM subjected to a frequency sweep (8 mm, 1–8 Hz)

The experimental study has yielded valuable insights into the effects of friction on the response. It has become evident that for a precise modeling of real-world applications with low-frequency elastodynamic metamaterials, the influence of friction, particularly static friction, must be taken into account. Furthermore, it has been demonstrated that damping resulting from 3D printed parts, necessitates high-order approximation modeling, as the linear model with viscous damping resulted to be inadequate.

6.5 Linear and Bistable Metafoundations

6.5.1 Basic Aspects of a Metafoundation

As underlined in the Sect. 6.1, locally resonant metamaterials (LRM) are commonly considered in the low-frequency regime, due to their ability to exhibit low-frequency bandgaps. The fundamental concept involves designing a periodic structure that possesses stop bands capable of prohibiting or attenuating the propagation of elastic waves within a desired frequency range. In particular, the metafoundation (MF) comprises a finite number of unit cells realized with a main frame and an internal moving reinforced concrete (RC) mass, that acts as a resonator. The main cell consists of two primary components: flexible columns and an RC slab, as depicted in Fig. 6.25b. The main cell serves two essential purposes: first, it must possess high flexibility to increase the structure's period, and second, it should have sufficient strength to support the substantial weight of the resonator blocks. The resonators are connected to the main frame slab through springs, as illustrated in Fig. 6.25b. There are various approaches for realizing these springs; however, wire ropes prove to be a suitable choice due to their three-dimensional flexibility and high damping capabilities (Basone et al. 2019b).

To demonstrate the performance, parameters, and characteristics of the MF, a slender petrochemical tank was chosen as a case study, as depicted in Fig. 6.26a. The tank compromises a radius of 8 and 24 m liquid height. Accordingly, the simplified

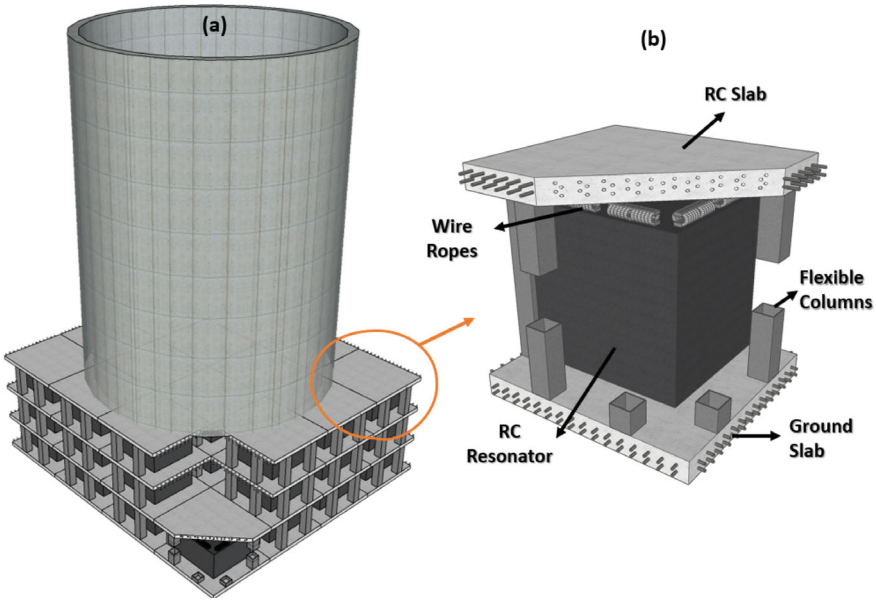

Fig. 6.25 **a** Triple layer metafoundation layout for slender storage tank; **b** Unit cell details

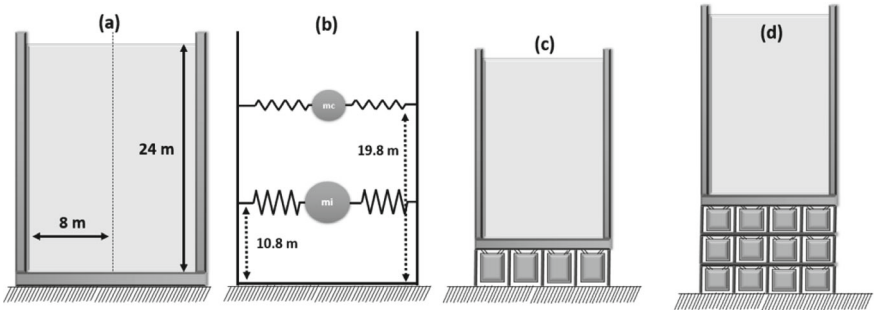

Fig. 6.26 Details of the superstructure and the MFs: **a** Slender petrochemical tank; **b** Simplified dynamical modelling of the tank; **c** Tank with a single layer MF; **d** Tank with a triple layer MF

Table 6.3 Details of the simplified tank model

Impulsive			Convective		
m_i	4014.8	Tons	m_c	762.4	Tons
c_i	5790.6	kNs/m	c_c	11.4	kNs/m
k_i	835184.1	kN/m	k_c	1717.7	kN/m

hydrodynamic response model suggested by Malhotra et al. (2000) that provides the correct dynamical superstructure response on the MF due to impulsive and convective masses is implemented. The properties of the simplified model are provided in Table 6.3 and presented in Fig. 6.26b. It can be seen that due to the slenderness of the tank, impulsive mass contributes a significantly larger mass ratio; accordingly, throughout the research, the results are given for the impulsive mass; nevertheless, the first convective mode is still included in the modelling and analysis stages.

To assess and standardize the performance of different MFs, a set of artificially generated ground motion (GM) records was utilized. These motions were generated in agreement with the Eurocode 8 (EC8) (European Committee for Standardization 2004b) response spectra (Mitseas and Beer 2019). The evaluation was conducted at locations with design peak ground accelerations (PGA) of 0.3, 0.5, and 0.7 g, with all locations assumed to have soil type B. To ensure a comprehensive analysis, time history simulations were carried out using 100 artificially generated horizontal accelerograms per location. The Newmark integration scheme—constant average acceleration—was employed for accurate numerical integration of EoMs (Fig. 6.27).

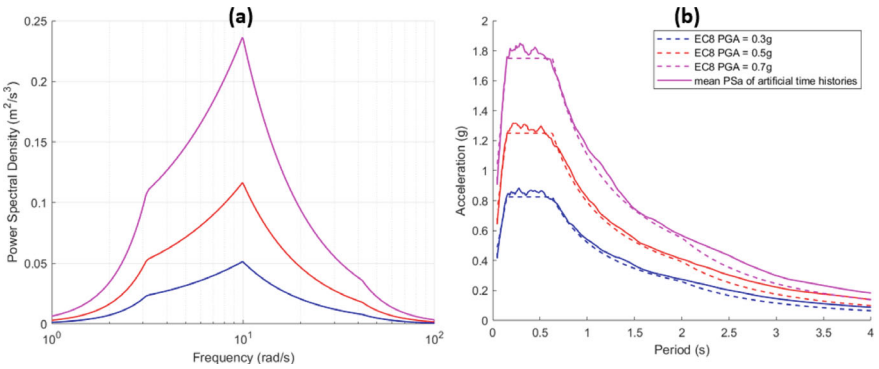

Fig. 6.27 **a** Single sided power spectral density of design spectra; **b** comparison of design spectra against mean spectra of artificially generated GMs

6.6 Linear Metafoundation

The MF combines the effects of conventional seismic isolation, tuned mass dampers, and low-frequency bandgaps effects of the LRM. Consequently, the performance of the MF is influenced by multiple parameters, which are thoroughly investigated and explained in the following sections.

6.6.1 Main Cell Parameters

To achieve maximum isolation effect, the columns of the main cell should be designed using the most flexible section that satisfies the design criteria. Several factors such as section type, material, number of columns (N_{col}), and column height (H_{col}) in a layer can influence the stiffness. The selection of section type and material depends on factors like availability, requirements, and the engineer's design choices. The number of columns can be determined based on the number of unit cells considered in a layer. Referring to Fig. 6.25b, the number of cells in the -X direction (N_{Cx}) and the -Y direction (N_{Cy}) affect theN_{col}. To understand the impact of N_{col}, multiple single-layer MFs were designed with different N_{Cx} values (assuming $N_{Cy} = N_{Cx}$). Figure 6.28a presents the variations in horizontal and vertical stiffness. It is observed that increasing N_{Cx} and N_{Cy} leads to lower stiffness in the horizontal direction but results in a stiffness increase in the vertical direction. Consequently, the determination of the number of cells creates a Pareto front optimization problem, which requires a trade-off between horizontal and vertical stiffness. The Pareto front plot is shown in Fig. 6.28b. The Pareto front represents the optimal horizontal and vertical stiffness values and the N_{Cx} can be selected either by a decision-maker considering additional factors or through methods such as the sum of weighted sums or the utopian point, as depicted in Fig. 6.28b.

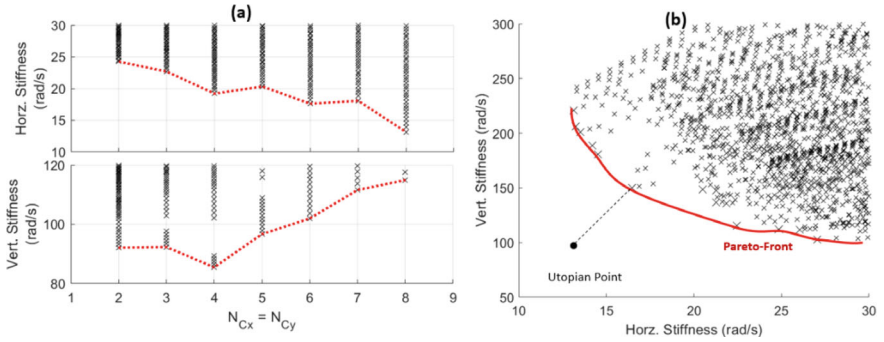

Fig. 6.28 Design results with various N_{Cx} $(= N_{Cy})$ values: **a** Variation of horizontal and vertical stiffness of the structure wrt N_{Cx} $(= N_{Cy})$; **b** Pareto front representation of horizontal and vertical stiffness values together with the optimum solution wrt the utopian point

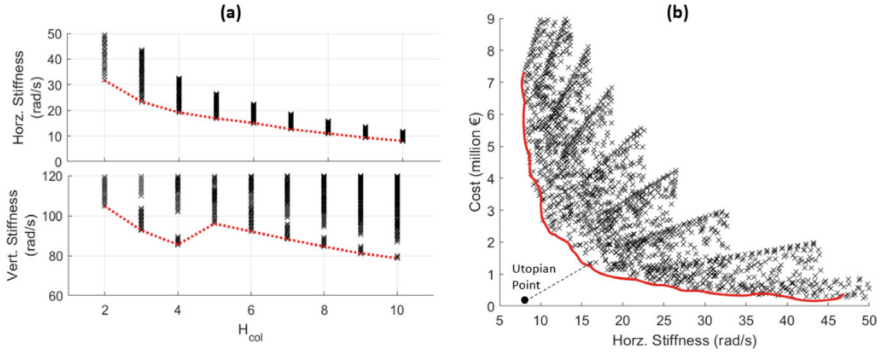

Fig. 6.29 Design results with various H_{col} values: **a** Variation of horizontal and vertical stiffness of the structure wrt H_{col}; **b** Pareto front representation of horizontal and vertical stiffness values together with the optimum solution wrt the utopian point

The height of the columns directly impacts the flexibility in both the horizontal and vertical directions. This aspect of the MF offers significant advantages, as the performance can be enhanced by adjusting the H_{col}. However, it is important to note that, as demonstrated by Guner et al. (2022), that due to the additional material and excavation costs involved, the cost of the MF rapidly increases as H_{col} increases. For economic viability, the cost of a single-layer MF and the corresponding horizontal flexibility for various column heights are presented in Fig. 6.29. Once again, it is evident that there is a trade-off between cost and flexibility, resulting in a Pareto front problem that requires either a decision or a logical algorithmic selection.

6.6.2 Resonator Parameters

In the case of a single-layer MF, the resonators act as tuned mass dampers for uncoupled translational degrees of freedom. Therefore, a vast body of background and parametric research on tuned mass dampers can readily be applied to the resonators of the MF. One crucial factor in designing the resonators is the determination of the resonator mass. Based on knowledge about tuned mass dampers, it is well-established that an increase of the resonator mass corresponds to an improve in performance. Hence, it is advisable to utilize the maximum mass of the resonator. It is worth noting that the size of the resonators depends on H_{col}, N_{Cx} and N_{Cy} assuming that the foundation size is fixed and determined by the dimensions of the superstructure. Therefore, there is a clear linear relationship between H_{col} and the total resonator mass in a layer (M_{Res}). Conversely, N_{Cx} and N_{Cy} have a reverse and nonlinear relationship, as an increase in the number of cells leads to an increase in N_{col}, reducing the available space for the resonators; refer to Fig. 6.30a, in this respect. Additionally, since each resonator requires a certain distance from the surrounding columns (see Fig. 6.25a), the decrease in M_{Res} increases as N_{Cx} and N_{Cy} grow. Together with the previous flexibility objectives, the 3D optimization problem can be shown as depicted in Fig. 6.30b. It can be seen that the utopian point exhibits the lowest stiffness values with the maximum resonator mass. For the current case, the closest point was determined at $N_{Cx} = N_{Cy} = 4$ and considered in the rest of the study.

The effectiveness of tuned mass dampers relies on properly tuning the resonator stiffness and damping parameters in relation to the characteristics of the superstructure. Numerous options and intelligent optimization procedures are available in the literature, although they are not elaborated upon in this context. In this research, a frequency-based H_∞ optimization procedure has been employed, which takes into

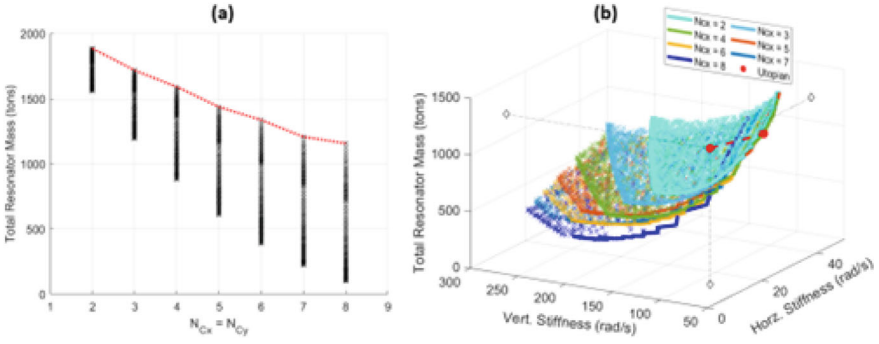

Fig. 6.30 Design results with various N_{Cx} $(= N_{Cy})$ values: **a** Variation of the total resonator mass in the MF wrt N_{Cx} $(= N_{Cy})$; **b** Pareto front representation of horizontal stiffness, vertical stiffness and total resonator mass values together with the optimum solution wrt to the utopian point. The optimum was located at $N_{Cx} = N_{Cy} = 4$

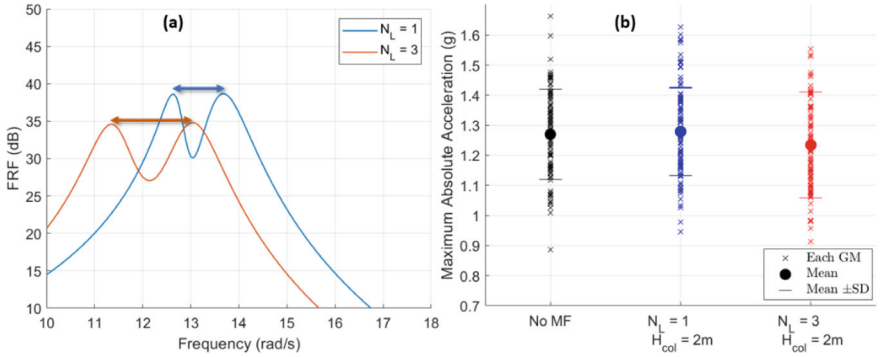

Fig. 6.31 Comparison of 2 and 6 m MFs with $N_L = 1$ and $N_L = 3$: **a** Frequency response functions behaviour; **b** Time history analysis results

account the site soil conditions through an input power spectral density (PSD) function (Guner et al. 2022). On the other hand, for nonlinear cases, where the system linearization is not feasible, the relevant optimization can be conducted in the time domain using methods such as design point selection (e.g., central composite design, Latin hypercube sampling) and surface fitting techniques like Kriging (Guner et al. 2023).

It is crucial to highlight that the MF incorporates multiple resonators, which can act in parallel, series, or complex coupling arrangements. This characteristic allows for the creation of wide ranges of attenuation due to locally resonant effects. Since earthquakes typically have a broad frequency content, a wider range of attenuation provides better protection and robustness against randomness. MFs with $N_L = 1$ and $N_L = 3$ were designed with the same $H_{col} = 2\,m$ and both frequency response functions and time history analyses results are presented in Fig. 6.31. With an increasing number of layers, the attenuation around the resonance frequency also increases, in terms of both amplitude and frequency range. However, since H_{col} was kept constant, the MF height increases. A similar investigation has been made by keeping the MF height the same at 6 m and considering two MFs with $N_L = 1$ and $N_L = 3$ ($H_{col} = 6$ and 2 m, respectively). The relevant results are presented in Fig. 6.32: one can observe that the increased layer stiffness in $N_L = 3$ results in a worst performance than the single-layer case.

6.7 Bistable Metafoundations

Although bistability was considered earlier for seismic isolation (Plaut et al. 2008; Jeffers et al. 2008), the protection focussed on the vertical component of seismic waves. In this respect, linear metafoundations have also been profitably proposed to mitigate the vertical motion of storage tanks and small modular reactors (Franchini

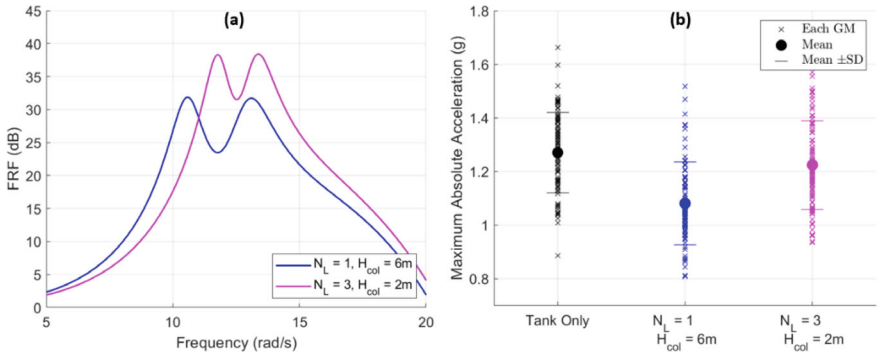

Fig. 6.32 Comparison of 6 m MFs with $N_L = 1$ and $N_L = 3$: **a** Frequency response functions; **b** Time history analyses results

et al. 2020; Guner et al. 2022). Conversely, the concept of combining bistability with Locally Resonant Metafoundations (MFs) devoted to the seismic isolation of process components against the horizontal component of waves is largely unexplored. To address this missing issue, four different MFs were designed with single and double layer configurations as well as endowed with linear and bistable columns. For clarity, the single-layer and the double-layer MFs are identified with the prefix 1L- and 2L-, respectively. Along this line, the structural details of the 2L-BM are depicted in Fig. 6.33. More precisely, each metafoundation cell consists of two parts: (i) the primary cell is composed of four flexible slender steel columns and two concrete slabs; (ii) the concrete resonator that is connected to the slab with steel wire ropes. The relevant design followed both Eurocode 1993 Part 1-1 (European Committee for Standardization 2005) and Eurocode 1998 Part 1 (European Committee for Standardization 2004a). The construction site was selected in Priolo Gargallo in Sicily, Italy, and is characterized by soil type B with peak ground acceleration (PGA) equal to 0.56 g for a return period of 2475 years. Each layer has a height H = 1 m and contains 9 unit cells in a 3 by 3 layout. The superstructure is a slender fuel unanchored storage tank that is a part of an existing plant (Salandra et al. 2017; Carta et al. 2016).

To introduce the bistability effect into the MFs, pre-buckled steel columns were conceived. In particular, columns were designed to elastically buckle due to gravity loading along their weak axis. The weight of the tank was assumed to be constant at its maximum capacity for the safe life limit state. The foundation is symmetric in the x and y axes; as a result, half of the columns are designed to buckle on the x-axis whilst the rest buckle on the y-axis. One of the critical points of the buckled columns is that once the buckling load is reached, the stable region where the column stiffness in the lateral direction is positive is comparatively small and sensitive to axial loading. To overcome this issue, the strong axis of the buckled columns was used as a restraining mechanism for lateral displacements of buckled columns. However, it is not favourable to add the strong axis stiffness of columns to the stiffness of

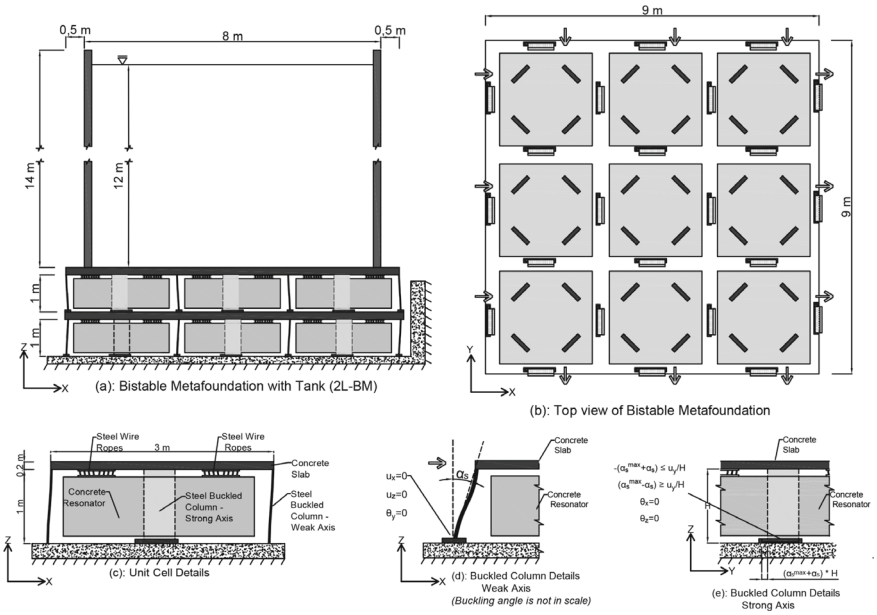

Fig. 6.33 **a** A bistable MF with a storage tank; **b** Top view of the bistable LRMF; **c** Unit cell details; **d** Weak axis view of a buckled column; **e** Strong axis view of a buckled column

the snap-through region. Consequently, the column ends are designed such that they allow unrestrained motion in the strong axis up to an amount of allowed snap-through buckling distance. In other words, between two stable points of weak axis buckled columns, there is no additional stiffness induced from the columns in the strong axis. However, in the case of a significant demand, the strong axis of the columns contributes to the lateral resistance and prevents instability.

Due to the coupled mechanism of buckling where the lateral stiffness is bound with axial load, the design of the columns becomes a challenging problem. In the design process, two main points were considered. In the weak axis, the columns should be weak enough and slender, with a slenderness ratio $L_e/r = 200$, to elastically buckle due to the superstructure load; but they should exhibit a high moment capacity, to remain elastic after buckling. Furthermore, in the strong axis, they must resist lateral loads. The selection of the steel column section was governed by weak axis limitations. In this respect, two parameters are important: the section width b and the flange thickness t_f; to minimize the buckling load, the weak axis moment of inertia must be reduced and depends on b^3 and t_f; to maximize the moment capacity, b^2 and t_f should be increased. As the effect of b is more prominent on the buckling load, t_f should increase to improve the moment capacity. Therefore, t_f is maximized, and the favourable section is the rectangular one.

Preliminary analyses carried out with rectangular sections, entailed that the allowed post-buckled drift angle α_s of the column, significantly influences the system response. The α_s value can be also defined as the drift angle of snap-through buckling range in both directions $(-\alpha_s, \alpha_s)$ or the drift angle that corresponds to half of the distance between stable points and reads,

$$\alpha_s = \arctan\left(\frac{u_{top}^{pb} - u_{bottom}^{pb}}{H}\right) \tag{6.11}$$

where u^{pb} represents the post-buckled displacement and H defines the storey height. This angle can be adjusted during the design stage by limiting the drift capability of the column using the strong axis allowance of the adjacent columns.

To present the benefits of the bistable MFs (BMs), also linear MFs (LMs) were designed and analyzed. The corresponding columns were designed to remain elastic and undamaged for the considered seismic design level; therefore, the hollow square steel sections were considered with a S355 steel grade. The dimensions of the designed cross sections are gathered in Table 6.4.

To achieve the best performance from each BM, an optimization process on some mechanical parameters is deemed necessary. The connection of the resonators to the primary cell is realized by means of linear springs and dashpots can be subject to optimization of the MFs. For each resonator mass, in view of efficiency, the largest mass compatible with the unit cell dimensions is taken (Reggio and Angelis 2015; Basone et al. 2019a). In addition to the resonator variables, the allowed snap-through buckling range $[0, \alpha_S^{max}]$ is also considered as an optimization parameter, where α_S^{max} is computed from the elastic limits of the column steel section. In fact, low α_s values trigger more snap-through motions, and this behaviour entails wanted energy dissipation. The performance index (PI) adopted in the optimization of the BM is the energy dissipation index (*EDI*), Basone et al. (2019a), that reads,

$$EDI = \frac{\sum E_d^{col} + \sum E_d^{res}}{\sum E_d^{col} + \sum E_d^{res} + E_d^{imp} + E_d^{con}} = \frac{\sum E_d^{col} + \sum E_d^{res}}{\sum E_d} \tag{6.12}$$

In particular, the EDI is defined as the ratio of dissipated energy by the LRMF with respect to the whole structure. Since all elements of the metastructure are elastic, and the bistable system exhibits no hysteretic dissipation, the energy can only

Table 6.4 Design column dimensions and parameters

LM	Layer	Width (mm)	Thickness (mm)	BM	Layer	Width (mm)	Depth (mm)	α_S^{max} deg
1L	1	130	30	1L	1	360	16	3
2L	1	160	30	2L	1	425	16	3
	2	150	30		2	385	16	3.3

be dissipated through viscous damping. The details of the optimization are available in Guner et al. (2023). To validate the optimized solutions, nonlinear time history analyses were carried out. For completeness, earthquakes associated with the design basis earthquake (DBE) and the safe shutdown earthquake (SSE) events were considered; moreover, the resonators were characterized by the optimized mechanical parameters.

In view of completeness, in addition to the EDI defined in Eq. (6.11), the seismic input energy provided to the superstructure E_{SS} is evaluated. E_{SS} can be computed as follows,

$$E_{SS} = m_i \cdot \int_0^{\tau} a_g(t) \cdot v_i(t) \cdot dt + m_c \cdot \int_0^{\tau} a_g(t) \cdot v_c(t) \cdot dt \tag{6.13}$$

where, m and v(t) define both mass and velocity whilst subscripts i and c identify impulsive and convective masses, respectively; $a_g\ (t)$, instead, defines the ground acceleration at time t, whilst τ defines the generic duration of each seismic record. Clearly, an efficient performance of the metafoundation limits the amount of E_{SS}.

Therefore, for each DBE and SSE limit state, eight seismic records were selected to assess the performance of the proposed LRMFs, respectively. The selected seismic records are collected in Table 6.5 whilst the acceleration spectra, their mean, and mean plus one standard variation are plotted in Fig. 6.34.

Herein, Fig. 6.35 depicts the EDI values for each seismic record of Table 6.5 both for the 1L and 2L LRMFs, respectively, with their median values. In both cases, the BM entails more than 10% increased median EDI values whilst keeping EDI value above 70% for all events. Clearly, there are a couple of SSE events where the 1L LM does not exhibit a favourable behaviour. Conversely, the 2L BM exhibit a favourable median EDI for both DBE and SSE events. Consequently, the bistable snap-through motions in the metafoundations cause an increased damping and prevent damage to the superstructure.

The advantages of the proposed bistable metastructures can be clearly appreciated through the estimate of E_{SS}. The results are depicted in Fig. 6.36 for both DBE and SSE events, respectively. In the case of a single layer, see Fig. 6.36a and c, given the large amounts of E_{SS}, the BM underperforms with respect to the LM in almost all cases. Though the 1L-BM is characterized by a favourable EDI, the energy dissipated in the BM is not enough. The 2L-BM instead, entails a different isolation effect due to the presence of 2 layers of bistable columns. More precisely, in the case of DBE events, the 2L-BM transfers only 6.1% of energy to the superstructure, in terms of median, compared to the 2L-LM case. With regard to the SSE events, see Fig. 6.36d, reductions of about 8.9% of E_{SS} in terms of median are achieved. Clearly, there are cases, the 1st and 3rd SSE event, where the 2L-BM underperformed with the high E_{SS}. The seismic records and their frequency content causes the 2L-BM to work outside of the snap-through region delimited by α_s. Therefore, the strong axis of the columns significantly contributes to the response, with an increase in stiffness and high energy transfer E_{SS}.

Table 6.5 List of selected seismic records and relevant parameters

DBE events	GM no.	Location	Country	Date	MW	Rjb (km)	PGA (g)
	1	Ano Liosia	Greece	07/09/1999	6	14	0.31
	2	South Iceland	Iceland	17/06/2000	6.5	15	0.48
	3	South I. (aftershock)	Iceland	21/06/2000	6.4	12	0.39
	4	L'Aquila Mainshock	Italy	06/04/2009	6.3	5	0.40
	5	L'Aquila Mainshock	Italy	06/04/2009	6.3	4	0.45
	6	L'Aquila Mainshock	Italy	06/04/2009	6.3	6	0.33
	7	L'Aquila Mainshock	Italy	06/04/2009	6.3	5	0.66
	8	Northridge-01	USA	17/01/1994	6.7	35	0.32
SSE events	GM no.	Location	Country	Date	MW	Rjb (km)	PGA (g)
	1	Erzincan	Turkey	13/03/1992	6.6	13.0	0.39
	2	South Iceland	Iceland	17/06/2000	6.5	7.0	0.63
	3	South Iceland	Iceland	21/06/2000	6.4	11.0	0.42
	4	L'Aquila	Italy	06/04/2009	6.3	4.6	0.44
	5	L'Aquila	Italy	06/04/2009	6.3	4.4	0.49
	6	L'Aquila	Italy	06/04/2009	6.3	4.9	0.55
	7	Landers	USA	28/06/1992	7.3	11.0	0.27
	8	Northridge-01	USA	17/01/1994	6.7	20.1	0.57

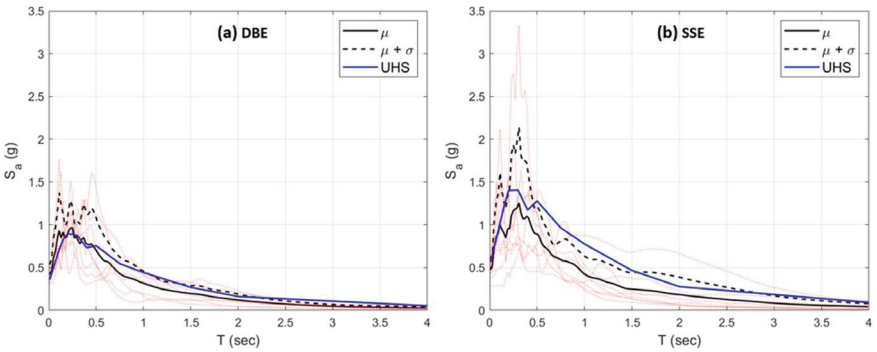

Fig. 6.34 Response spectra of the selected seismic records: **a** DBE limit state; **b** SSE limit state

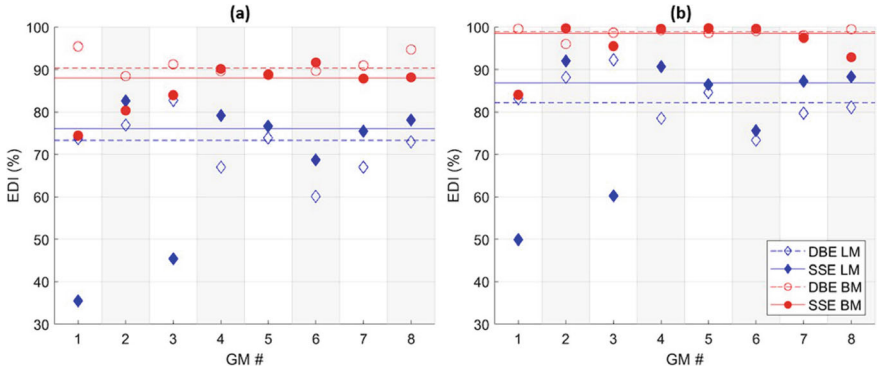

Fig. 6.35 EDI results for each seismic record collected in Table 6.5, where the solid and dashed lines represent the median for SSE and DBE events, respectively: **a** 1L LRMFs case; **b** 2L LRMFs case

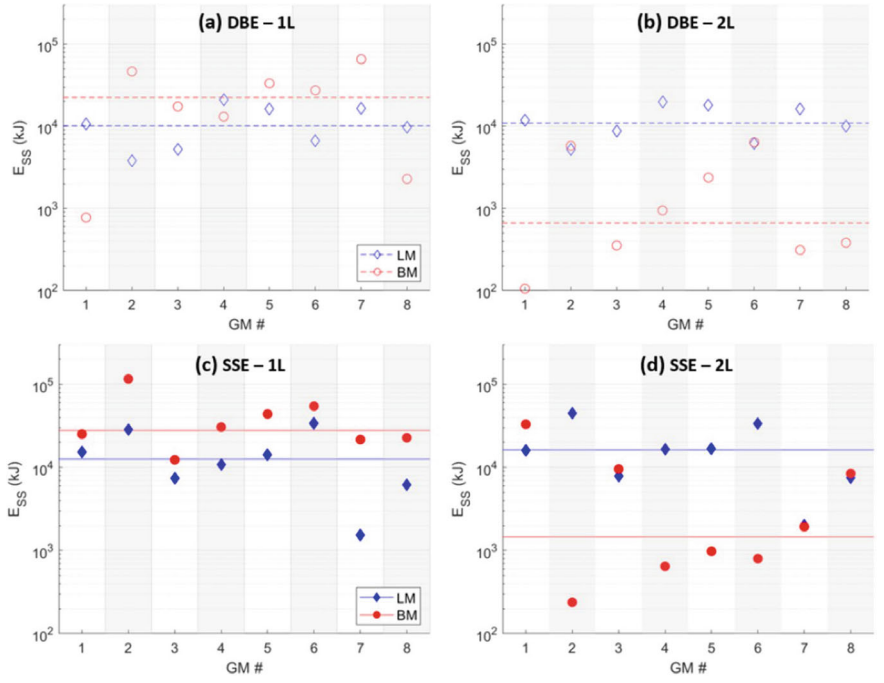

Fig. 6.36 Plots of the energy E_{SS} transferred to the superstructure for the seismic records of 6.5. Continuous lines define median values: **a** DBE-1L case; **b** DBE-2L case; **c** SSE-1L case; **d** SSE-2L case

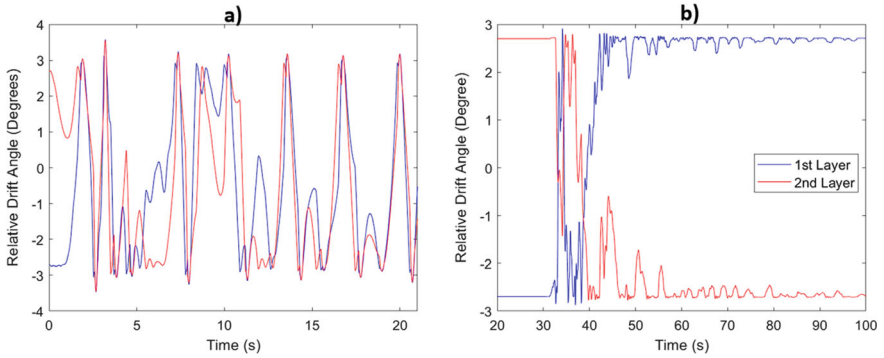

Fig. 6.37 Time history relative drift angle responses of the 2L-BM main slabs: **a** SSE GM-1 record; **b** SSE GM-5 record

The time history displacement responses of the main slabs relevant to the 2L-BM in terms of relative drift angle are depicted in Fig. 6.37 for the GM-1 and the GM-5 SSE seismic records—1992 Erzincan and 2009 L'Aquila events of Table 6.5. The first event entails the worst case for the 2L-BM and the 2L-LM performs better. In particular, from Fig. 6.37a, one can argue that the first layer switches from the starting position to the other stable point and then, both layers move in a synchronized manner. Therefore, both layers act together rather than creating asymmetric modes. In particular, the GM-1 record excites low-frequency modes where both layers move together and the energy transfer to the superstructure increases. The opposite behaviour can be observed in Fig. 6.37b, where both layers vibrate and even columns buckle from one stable point to the other one, simultaneously, in opposite directions. This type of motion shows that the movement of the first layer slab governs and, simultaneously, excites the connected resonators with significant energy dissipation.

Time history analyses conducted on optimized bistable metafoundations (BMs) highlighted the favourable behaviour of these isolation systems in terms of reduction of the total seismic energy input transferred to the superstructure. Clearly, the nonlinearity that characterizes the bistable mechanism significantly reduces the total structure stiffness and results in more compact locally resonant metafoundations wrt to the linear metafoundations.

6.8 Conclusions and Future Perspectives

6.8.1 Conclusions

An innovative methodology for the assessment of state-dependent fragility functions has been proposed. It is based on the combination of advanced surrogate modelling techniques, like bootstrapped-PCE, with data from FE models or real world to yield

state-dependent fragilities. These fragility curves are functions of the selected IM, and the initial damage condition limit state. The proposed method has been applied to a vertical tank of a more realistic industrial substructure archetype, comprehensively tested by means of a shaking table. The application to a complex and realistic industrial case study has allowed for the derivation of state-dependent fragility curves for a component that proved to be critical during the experimental campaign: the vertical tank mounted on the first floor of the 3-storey braced frame industrial steel structure. Through the estimation of the efficiency index, β_{eff}, it was possible to identify, among the optimal IMs, the relevant occurrence of the E ASAR67. This IM is of particular interest, since it considers the damage experienced by the system through a frequency range shift. Successively, empirical fragility curves were derived by leveraging the large number of outputs generated from the bootstrap and PCE combination. The best probability distribution was then inferred by employing the maximum likelihood estimation method and the Akaike information criterion.

With the aim of improving the performance of locally resonant metafoundations, bistability-based nonlinearities were introduced in the primary cells. The bistability was governed by elastically buckled steel columns, that can freely snap-through from one stable point to another. Along this line, an optimization framework based on the Central Composite Design and Kriging was proposed and utilized to optimize both resonator linear spring and damper properties and allowed bistable column snap-through distance. Time history analyses conducted on optimized bistable metafoundations (BMs) highlighted the favourable behaviour of these isolation systems in terms of reduction of the total seismic energy input transferred to the superstructure. Clearly, the nonlinearity that characterizes the bistable mechanism significantly reduced the total structure stiffness and resulted in a more compact locally resonant metafoundations wrt to the linear metafoundations. To further explore the dynamics and investigate the underlying properties of the bistable metafoundation (BM), the uncoupled single cell, the finite lattice and a periodic chain system of BM unit cells was investigated. Sinusoidal driven boundary inputs were applied to all systems and both time/frequency domain responses were obtained. The single cell analysis clearly showed the harmonic diffusion property. In addition, the harmonic diffusion of the antiresonance features of the resonators was also observed. The possibility of aperiodic motions were also discovered. Then, the energy transfer through finite chains was investigated by finite lattices. It has been shown that in both short and long input durations, the bistable finite lattices prevent energy transfer by snap-through motions with <10 cells. Moreover, as the input duration increases, the energy transferred to the generic cell significantly differs between the bistable and linear finite lattices; and the bistable lattice outperforms. In addition, the dispersion relations of the bistable periodic system have been computed using both analytical and numerical tools. The analytical results obtained through the harmonic balance method showed a very good agreement with the numerical approach based on the 2D FFT. Thus, the dispersion properties of the nonlinear system have been quantified.

6.8.2 Future Perspectives

With regard to the fragility assessment of industrial substructures, further analysis of other system configurations are needed, to enhance and generalise the aforementioned findings. Moreover, based on proper assumptions, the state-depend fragility curves derived from critical industrial substructures could populate Markovian transition matrices, very useful for the quantification of restoring functions.

As far as metafoudations are concerned, the complex dynamics related to bistability and wire rope hysteresis deserve further studies. More specifically, the effects of varying gravitational loads, vertical seismic excitations together with the physical realization of wire ropes and a finite lattice with the control of parameters that accurately replicate bistable nonlinear components warrants further research.

References

17-917-44 NISTGCR. (2017). Seismic analysis, design, and installation of nonstructural components and systems—Background and recommendations for future work.

Arrieta, A. F., Hagedorn, P., Erturk, A., & Inman, D. J. (2010). A piezoelectric bistable plate for nonlinear broadband energy harvesting. *Applied Physics Letters, 97*(10).

Basone, F., Wenzel, M., Bursi, O. S., & Fossetti, M. (2019a). Finite locally resonant metafoundations for the seismic protection of fuel storage tanks. *Earthquake Engineering & Structural Dynamics, 48*.

Basone, F., Wenzel, M., Bursi, O. S., & Fossetti, M. (2019). Finite locally resonant metafoundations for the seismic protection of fuel storage tanks. *Earthquake Engineering and Structural Dynamics, 48*, 232–252.

Bursi, O. S., Basone, F., & Wenzel, M. (2021a). Stochastic analysis of locally resonant linear and hysteretic metamaterials for seismic isolation of process equipment. *Journal of Sound and Vibration, 510*, 116263.

Bursi, O. S., Basone, F., & Wenzel, M. (2021b). Stochastic analysis of locally resonant linear and hysteretic metamaterials for seismic isolation of process equipment. *Journal of Sound and Vibration, 510*. https://doi.org/10.1016/j.jsv.2021.116263

Carta, G., Movchan, A. B., Argani, L. P., & Bursi, O. S. (2016). Quasi-periodicity and multi-scale resonators for the reduction of seismic vibrations in fluid-solid systems. *International Journal of Engineering Science, 109*.

Cazottes, P., Fernandes, A., Pouget, J., & Hafez, M. (2009, September). Bistable buckled beam: Modeling of actuating force and experimental validations. *Journal of Mechanical Design, 131*(10), 101001. ISSN 1050-0472. https://doi.org/10.1115/1.3179003

Celli, P., Yousefzadeh, B., Daraio, C., & Gonella, S. (2019). Bandgap widening by disorder in rainbow metamaterials. *Applied Physics Letters, 114*(9).

De Biasio, M., Grange, S., Dufour, F., Allain, F., & Petre-Lazar, I. (2015). Intensity measures for probabilistic assessment of non-structural components acceleration demand. *Earthquake Engineering & Structural Dynamics*. https://doi.org/10.1002/eqe.2582

Dubnau, D., & Losick, R. (2006). Bistability in bacteria. *Molecular Microbiology, 61*(3), 564–572.

Durstewitz, D., & Seamans, J. K. (2006). Beyond bistability: Biophysics and temporal dynamics of working memory. *Neuroscience, 139*(1), 119–133.

European Committee for Standardization. (2004a). Design of structures for earthquake resistance—Part 1: General rules, seismic actions and rules for buildings. Eurocode 8-1.

European Committee for Standardization. (2004b). Design of structures for earthquake resistance—Part 1: General rules, seismic actions and rules for buildings. Eurocode 8-1, CEN/TC 250, Brussels.

European Committee for Standardization. (2005). Design of steel structures. Part 1-1: General rules and rules for buildings. Eurocode 3-1-1.

Fajfar, P., Vidic, T., & Fischinger, M. (1990). A measure of earthquake motion capacity to damage medium-period structures. *Soil Dynamics and Earthquake Engineering, 9*(5), 236–242. https://doi.org/10.1016/S0267-7261(05)80002-8

Franchini, A., Bursi, O. S., Basone, F., & Sun, F. (2020). Finite locally resonant metafoundations for the protection of slender storage tanks against vertical ground accelerations. *Smart Materials and Structures, 29*, 5. https://doi.org/10.1088/1361-665X/ab7e1d

Frazier, M. J., & Kochmann, D. M. (2017). Band gap transmission in periodic bistable mechanical systems. *Journal of Sound and Vibration, 388*, 315–326.

Gammaitoni, L., Marchesoni, F., Menichella-Saetta, E., & Santucci, S. (1989). Stochastic resonance in bistable systems. *Physical Review Letters, 62*(4), 349.

Giaralis, A., & Petrini, F. (2017). Wind-induced vibration mitigation in tall buildings using the tuned mass-damper-inerter (TMDI). *Journal of Structural Engineering, 143*(9), 04017127.

Guner, T., Bursi, O. S., & Broccardo, M. (2023). Seismic vibration mitigation of steel storage tanks by metafoundations endowed with linear and bistable columns. *Bulletin of Earthquake Engineering*, 1–26.

Guner, T., Bursi, O. S., Erlicher, S. (2022). Optimization and performance of metafoundations for seismic isolation of small modular reactors. *Computer-Aided Civil and Infrastructure Engineering*.

Habib, G., & Romeo, F. (2017). The tuned bistable nonlinear energy sink. *Nonlinear Dynamics, 89*(1), 179–196.

Hariri-Ardebili, M. A., & Saouma, V. E. (2016). Probabilistic seismic demand model and optimal intensity measure for concrete dams. *Structural Safety, 59*, 67–85. https://doi.org/10.1016/j.strusafe.2015.12.001

Harne, R. L., & Wang, K. W. (2013). A review of the recent research on vibration energy harvesting via bistable systems. *Smart Materials and Structures, 22*(2), 023001.

Hopf, F. A., Kaplan, D. L., Gibbs, H. M., & Shoemaker, R. L. (1982). Bifurcations to chaos in optical bistability. *Physical Review A, 25*(4), 2172.

Hussein, M. I., & Frazier, M. J. (2013). Metadamping: An emergent phenomenon in dissipative metamaterials. *Journal of Sound and Vibration, 332*(20), 4767–4774.

Hussein, M. I., Leamy, M. J., & Ruzzene, M. (2014). Dynamics of phononic materials and structures: Historical origins, recent progress, and future outlook. *Applied Mechanics Reviews, 66*. https://doi.org/10.1115/1.4026911

Iervolino, I., Giorgio, M., & Chioccarelli, E. (2015b). Markovian modeling of seismic damage accumulation. *Earthquake Engineering & Structural Dynamics, 45*, 441–461. https://doi.org/10.1002/eqe.2668.

Jeffers, A. E., Plaut, R. H., & Virgin, L. N. (2008). Vibration isolation using buckled or pre-bent columns—part 2: three-dimensional motions of horizontal rigid plate. *Journal of Sound and Vibration, 310*.

Knapen, T., Brascamp, J., Pearson, J., van Ee, R., & Blake, R. (2011). The role of frontal and parietal brain areas in bistable perception. *Journal of Neuroscience, 31*(28), 10293–10301.

Laura Eads, Eduardo Miranda, Helmut Krawinkler, and Dimitrios G Lignos. An efficient method for estimating the collapse risk of structures in seismic regions. *Earthquake Engineering & Structural Dynamics*, 42(1):25–41, 2013.

Liu, C., Chen, L., Lee, H. P., Yang, Y., & Zhang, X. (2022). A review of the inerter and inerter-based vibration isolation: Theory, devices, and applications. *Journal of the Franklin Institute*.

Lorenz, E. (2000). The butterfly effect. *World Scientific Series on Nonlinear Science Series A, 39*, 91–94.

Ma, R., Bi, K., & Hao, H. (2021). Inerter-based structural vibration control: a state-of-the-art review. *Engineering Structures, 243*, 112655.

Maldovan, A. (2013). Sound and heat revolutions in phononics. *Nature, 503*, 209–217.

Malhotra, P. K., Wenk, T., & Wieland, M. (2000). Simple procedure for seismic analysis of liquid-storage tanks. *Structural Engineering International, 10*(3), 197–201.

Marian, L., & Giaralis, A. (2017). Optimal design of a novel tuned mass-damper-inerter (TMDI) passive vibration control configuration for stochastically support-excited structural systems. *Probabilistic Engineering Mechanics, 38*, 156–164.

Miniaci, M., Krushynska, A., Bosia, F., & Pugno, N. M. (2016). Large scale mechanical metamaterials as seismic shields. *New Journal of Physics, 18*(8), 083041.

Mitseas, I. P., & Beer, M. (2019). Modal decomposition method for response spectrum based analysis of nonlinear and non-classically damped systems. *Mechanical Systems and Signal Processing, 131*, 469–485.

Nardin, C., Bursi, O. S., Paolacci, F., Pavese, A., & Quinci, G. (2022). Experimental performance of a multi-storey braced frame structure with non-structural industrial components subjected to synthetic ground motions. *Earthquake Engineering & Structural Dynamics, 51*(9), 2113–2136. https://doi.org/10.1002/eqe.3656

Palermo, A., Krödel, S., Marzani, A., & Daraio, C. (2016). Engineered metabarrier as shield from seismic surface waves. *Scientific Reports, 6*(1), 1–10.

Phan, H. N., Paolacci, F., Di Filippo, R., & Bursi, O. S. (2020). Seismic vulnerability of above-ground storage tanks with unanchored support conditions for NA-tech risks based on Gaussian process regression. *Bulletin of Earthquake Engineering, 18*, 6883–6906.

Plaut, R. H., Favor, H. M., Jeffers, A. E., & Virgin, L. N. (2008). Vibration isolation using buckled or pre-bent columns—Part 1: Two-dimensional motions of horizontal rigid bar. *Journal of Sound and Vibration, 310*.

Quinci, G., Nardin, C., Paolacci, F., & Bursi, O. S. (2023). Modelling issues in seismic risk analysis of non-structural components located on industrial plant subsystems. *Bulletin Earthquake Engineering, 02*. https://doi.org/10.1002/eqe.1132

Reggio, A., Angelis, M. D. (2015). Optimal energy-based seismic design of non-conventional tuned mass damper (TMD) implemented via inter-story isolation. *Earthquake Engineering & Structural Dynamics, 44*.

Rezaeian, S., & Der Kiureghian, A. (2010). Simulation of synthetic ground motions for specified earthquake and site characteristics. *Earthquake Engineering & Structural Dynamics*. https://doi.org/10.1002/eqe.997

Rossi, L., Stupazzini, M., Parisi, D., Holtschoppen, B., Ruggieri, G., & Butenweg, C. (2020). Empirical fragility functions and loss curves for Italian business facilities based on the 2012 Emilia-Romagna earthquake official database. *Bulletin of Earthquake Engineering, 18*, 1693–1721.

Rothos, V. M., & Vakakis, A. F. (2009). Dynamic interactions of traveling waves propagating in a linear chain with an local essentially nonlinear attachment. *Wave Motion, 46*(3), 174–188.

Saif, M. T. A. (2000). On a tunable bistable mems-theory and experiment. *Journal of Microelectromechanical Systems, 9*(2), 157–170.

Salandra, V., Wenzel, M., Bursi, O. S., Carta, G., & A. B. Movchan. Conception of a 3d metamaterial-based foundation for static and seismic protection of fuel storage tanks. *Frontiers in Materials, 4*.

Smith, M. C. (2002). Synthesis of mechanical networks: the inerter. *IEEE Transactions on Automatic Control, 47*(10), 1648–1662.

Specker, T., Buchholz, M., & Dietmayer, K. (2014). A new approach of dynamic friction modelling for simulation and observation. *IFAC Proceedings Volumes, 47*(3), 4523–4528.

Vathi, M., Karamanos, S., Kapogiannis, I., & Spiliopoulos, K. (2017, July). Performance criteria for liquid storage tanks and piping systems subjected to seismic loading. *Journal of Pressure Vessel Technology, 139*. https://doi.org/10.1115/1.4036916

Wenzel, M., Bursi, O. S., & Antoniadis, I. (2020). Optimal finite locally resonant metafoundations enhanced with nonlinear negative stiffness elements for seismic protection of large storage tanks. *Journal of Sound and Vibration, 483*. https://doi.org/10.1016/j.jsv.2020.115488